Materials Advances

ROYAL SOCIETY OF CHEMISTRY

PAPER

View Article Online
View Journal



Cite this: DOI: 10.1039/d6ma00325g

# Thermomechanical and energetic coupling in DVB-based copolymers: a unified physicochemical study of adsorption distance, surface energy, and specific surface area

Tayssir Hamieh [abc]

The adsorption behavior of organic probe molecules on DVB-based copolymers and hyper-cross-linked resins was investigated by inverse gas chromatography using a thermomechanical framework that explicitly couples adsorption energetics with temperature and specific surface area. Retention measurements performed over a broad temperature range enabled the determination of Gibbs free energies of adsorption, which were further decomposed into dispersive contributions governed by London interactions. The intermolecular separation distance between probe molecules and polymer surfaces was shown to obey a universal thermomechanical law, exhibiting a bilinear dependence on temperature and copolymer specific surface area. This behavior reveals that surface morphology acts as a direct control parameter of adsorption dilation rather than a purely geometric descriptor. The London dispersive surface energy of the copolymers displayed a systematic temperature dependence consistent with fundamental dispersion-interaction scaling. Importantly, the surface-area derivative of the dispersive surface energy followed a strict linear temperature law, demonstrating intrinsic coupling between thermal agitation and accessible surface morphology. Enthalpy–entropy compensation analysis further revealed that the intrinsic compensation temperature and enthalpic reference state are deterministic functions of specific surface area, leading to a generalized morphology-resolved compensation framework. The quadratic specific surface area scaling of compensation parameters provides direct experimental evidence that adsorption thermodynamics on polymeric networks are governed by thermomechanical constraints imposed by cross-linking architecture. These results establish a unified methodology for extracting physically meaningful surface parameters of polymeric solids, offering a molecular-scale interpretation of adsorption distances, dispersive surface energetics, and morphology-dependent thermodynamic invariants.

Received 7th March 2026,
Accepted 20th May 2026

DOI: 10.1039/d6ma00325g

rsc.li/materials-advances



## 1. Introduction

The physicochemical characterization of polymer and copolymer surfaces remains a central issue in interfacial thermodynamics, adsorption science, and materials engineering. Cross-linked copolymers derived from divinylbenzene (DVB) and chlorinated divinylbenzene (CDVB) are widely used in adsorption, chromatographic separations, catalysis, and molecular recognition due to their structural rigidity, high cross-link density, and tunable porosity. Despite their technological importance, a comprehensive thermodynamic description of their surface properties remains challenging because polymeric solids inherently exhibit energetic heterogeneity, structural disorder, and temperature-dependent molecular responses.[1–14]

Inverse gas chromatography at infinite dilution (IGC-ID) has progressively emerged as one of the most powerful techniques for investigating surface energetics of polymers and copolymers.[7–18] Unlike macroscopic methods such as contact-angle measurements, IGC probes molecular-scale interactions and provides direct access to fundamental thermodynamic quantities, including the free energy of adsorption, London dispersive surface energy, and specific (acid–base) interaction parameters.[10–14] Over the past decades, IGC has been successfully applied to a broad range of polymeric systems, including styrenic copolymers, elastomers, functional polymers, block copolymers, and highly cross-linked resins.[1–14]

A major strength of IGC lies in its ability to deconvolute dispersive and specific contributions to adsorption. The theoretical

[a] Faculty of Science and Engineering, Maastricht University, P.O. Box 616, 6200 MD Maastricht, The Netherlands. E-mail: t.hamieh@maastrichtuniversity.nl
[b] Institut de Science des Matériaux de Mulhouse, Université de Haute-Alsace, CNRS, IS2M UMR 7361, F-68100 Mulhouse, France
[c] Laboratory of Materials, Catalysis, Environment and Analytical Methods Laboratory (MCEMA), Faculty of Sciences, Lebanese University, Hadath, Lebanon

foundations for interpreting dispersive interactions originate from the work of Fowkes and Dorris–Gray, who established the relationship between retention behavior and London dispersive surface energy.[11–29] Subsequent developments extended IGC analyses to polar interactions, allowing the quantification of donor–acceptor surface properties of polymeric solids.[7–29] Numerous studies have demonstrated that IGC can sensitively capture subtle variations in polymer surface energetics arising from chemical modification, cross-linking degree, and molecular architecture.[1–14]

However, despite its success, important conceptual limitations remain in conventional IGC treatments. Classical approaches often assume temperature-independent adsorption geometries, uniform interaction potentials, and purely energetic interpretations of retention data.[20–29] Such assumptions can be problematic for cross-linked copolymers, where adsorption events are intrinsically coupled to local structural relaxation, surface deformation, and temperature-driven configurational fluctuations.[30–54] In rigid and hyper-cross-linked DVB-based networks, adsorption cannot be described solely by static interaction energies; instead, it involves a coupled thermodynamic–mechanical response of the polymer surface.[30–45]

Another unresolved issue concerns the role of specific surface area (SSA) in adsorption thermodynamics. Although SSA ($\mathcal{S}$) is routinely used as a structural descriptor of porous polymers and resins, its explicit coupling with adsorption energetics and temperature sensitivity is rarely addressed within a unified framework.[55–58] Traditional interpretations implicitly assume that $\mathcal{S}$ modifies adsorption magnitudes without fundamentally altering thermodynamic relationships. Yet, both theoretical considerations and experimental observations suggest that surface morphology and accessible area can significantly influence intermolecular distances, dispersive forces, and specific interactions.[55–62]

Recent advances have proposed a thermomechanical interpretation of adsorption on polymeric solids, in which the adsorption distance between probe molecules and surfaces becomes an experimentally meaningful variable.[55–62] Within this perspective, adsorption induces reversible local deformations and stress redistribution, leading to measurable temperature-dependent variations of intermolecular separation. This description introduces an effective thermal expansion parameter characterizing probe–surface coupling and provides a direct bridge between adsorption thermodynamics and polymer mechanics.[59–62] Such concepts are particularly relevant for highly cross-linked copolymers, where surface energetics are strongly influenced by temperature-dependent structural responses.

In the present work, we extend this thermomechanical–thermodynamic framework to a family of DVB- and CDVB-based copolymers, including poly(CDVB)–DCE, poly(CDVB)–NB, poly(DVB)–DCE, poly(DVB)–NB, and poly(DVB). Using inverse gas chromatography combined with an advanced Hamieh-type methodology,[55–62] we determine the free energy, dispersive energy, and polar energy of adsorption for a comprehensive set of organic probe molecules. This methodology departs fundamentally from classical treatments by explicitly incorporating the temperature dependence of adsorption distance and by systematically coupling adsorption parameters with specific surface area.

A central outcome of this approach is the demonstration that adsorption distances exhibit bilinear dependencies on temperature and SSA, revealing a direct morphology–temperature coupling not captured by traditional IGC models. Furthermore, the London dispersive surface energy displays bilinear behavior, while solvent molecular surface areas show linear and second-order variations, indicating a non-trivial coupling between adsorption thermodynamics and probe geometry.[59–62]

Beyond parameter determination, the analysis of enthalpy–entropy compensation relationships uncovers unexpected scaling correlations between distinct copolymer families. After centralization and normalization, adsorption enthalpies and entropies collapse onto quasi-universal linear relations, suggesting that solvent-induced thermodynamic fluctuations are governed by common underlying mechanisms across chemically distinct DVB-based networks. These findings provide new physical insight into how polymer morphology, accessible surface area, and thermodynamic response are intrinsically interconnected.

Overall, this work establishes a unified thermomechanical–thermodynamic description of solvent adsorption on cross-linked copolymers, offering improved accuracy in the determination of surface parameters and clarifying the fundamental role of temperature and surface morphology in polymer–probe interactions.

# 2. Experimental

## 2.1. Materials and solvents

**2.1.1. Copolymer structural characteristics.** The DVB-based polymer samples used in this study were commercial materials obtained from Sigma-Aldrich. They correspond to well-known classes of cross-linked aromatic polymers, including poly(styrene-divinylbenzene) (CAS 9003-70-7) and poly(vinylbenzyl chloride-divinylbenzene) (CAS 25085-82-3).

These base materials were further subjected to post-treatment using dichloroethane (DCE) and nitrobenzene (NB), following classical modification procedures for cross-linked polymer networks. Such treatments induce structural reorganization and additional cross-linking within the polymer matrix, leading to modifications of porosity, specific surface area, and adsorption properties.

Although commercial samples may differ in cross-linking density and morphology, all relevant physicochemical properties in the present study were determined experimentally by inverse gas chromatography, ensuring that the analysis reflects intrinsic material behavior.

*2.1.1.1 Monomer composition and network structure.* Poly(DVB) is formed by radical polymerization of divinylbenzene monomers, which act both as the primary structural units and as cross-linking agents due to their bifunctional vinyl groups. As a result, the polymer network is intrinsically cross-linked, leading to a rigid three-dimensional aromatic framework.

In the case of poly(CDVB), chloromethylated DVB precursors are used, enabling subsequent post-cross-linking reactions. The chloromethyl functional groups serve as reactive sites for internal Friedel–Crafts-type cross-linking, resulting in a significant increase in network connectivity and the formation of hyper-cross-linked structures.

*2.1.1.2 Cross-linking density.* The cross-linking density in DVB-based polymers is inherently high due to the bifunctional nature of the DVB monomer. In hyper-cross-linked poly(CDVB) systems, the effective cross-linking density is further increased through post-cross-linking reactions, leading to:

- enhanced rigidity of the polymer framework,
- reduced segmental mobility,
- increased development of microporosity.

Although the exact cross-linking density depends on synthesis conditions, these materials are typically characterized by highly cross-linked aromatic networks, where the density of cross-links directly governs the accessibility and distribution of adsorption sites.

*2.1.1.3 Modification degree (post-cross-linking treatments).* Post-cross-linking using solvents such as DCE and NB induces internal network rearrangements through solvent-assisted swelling followed by cross-link formation. These treatments result in:

- an increase in the number of effective cross-linking bridges,
- a reorganization of the pore structure,
- modification of the accessible surface area.

The degree of modification depends on the extent of swelling and the reactivity of the system, but it generally leads to hyper-cross-linked structures with significantly enhanced specific surface areas compared to the parent poly(DVB).

*2.1.1.4 Particle size and morphology.* The polymer samples are typically obtained in granular or spherical form, with particle sizes ranging from approximately: 50 to 500 μm depending on synthesis and processing conditions.

At the microscopic level, these particles exhibit:

- irregular internal morphology,
- interconnected pore networks,
- heterogeneous distribution of adsorption sites.

The external particle size has a negligible direct influence on adsorption thermodynamics under infinite dilution conditions but plays a role in ensuring uniform packing and reproducible chromatographic measurements.

*2.1.1.5 Porosity and pore structure.* DVB-based copolymers and hyper-cross-linked resins are characterized by a predominantly microporous structure, with pore sizes typically below 2 nm. In addition, depending on the synthesis and post-cross-linking treatment, a contribution from mesoporosity (2–50 nm) may also be present.

The porosity originates from:

- the rigid aromatic backbone,
- the high cross-linking density,
- the solvent-induced network expansion during post-cross-linking.

This results in a complex pore architecture combining:

- micropores, responsible for strong adsorption interactions,
- mesopores, facilitating molecular accessibility.

*2.1.1.6 Specific surface area (SSA).* The specific surface area of the investigated materials, determined experimentally (Table S1), reflects the accessible internal surface available for adsorption. In hyper-cross-linked DVB-based systems, SSA values typically range from 500 to 1500 $m^2\ g^{-1}$ depending on the degree of cross-linking and post-cross-linking treatment.

Importantly, in the present work, SSA is not treated solely as a geometric descriptor but as a thermodynamic variable that directly influences adsorption distance, surface energy, and enthalpy–entropy compensation behavior.[10–14,63]

All copolymer samples were obtained in particulate form (from Sigma-Aldrich, France) and were used as received without further chemical treatment. Prior to inverse gas chromatography (IGC) measurements, the materials were conditioned under controlled thermal and vacuum conditions to remove any physically adsorbed contaminants and residual volatiles. This pre-conditioning step ensured reproducible surface states and minimized interference from adventitious adsorption.

**2.1.2. Solvents.** The probe molecules employed in the inverse gas chromatography experiments consisted of a homologous series of *n*-alkanes and a representative set of polar organic solvents (from Sigma-Aldrich, France). The *n*-alkanes (*n*-pentane, *n*-hexane, *n*-heptane, *n*-octane, and *n*-nonane) were used to characterize London dispersive interactions. The polar probes included carbon tetrachloride, nitromethane, dichloromethane, trichloromethane (chloroform), diethyl ether, tetrahydrofuran (THF), ethyl acetate, acetone, acetonitrile, methanol, ethanol, toluene, benzene, and cyclohexane. This selection provided a broad distribution of molecular sizes, polarizabilities, and polar surface properties, enabling comprehensive analysis of dispersive and specific adsorption contributions. Dichloroethane (DCE) and nitrobenzene (NB) were additionally employed as post-cross-linking solvents for the modification of DVB-based copolymers. These solvents are known to promote internal rearrangement and network densification in cross-linked aromatic polymers, thereby influencing porosity and adsorption properties. They were not used as chromatographic probes.

All solvents were of high-purity analytical grade (typically $\geq$99%) and were used without additional purification. The purity of probe molecules was verified according to supplier specifications to ensure reliable retention measurements. Helium (high-purity grade) was employed as the carrier gas for all IGC experiments. Some experimental data used in this work were obtained from several previous studies.[10–14,63]

## 2.2. Inverse gas chromatography measurements

Inverse gas chromatography experiments were performed under infinite dilution conditions using a surface energy analyzer equipped with a flame ionization detector (FID). High-purity helium was employed as the carrier gas, ensuring inert

transport of probe molecules and minimizing secondary interactions. The carrier gas flow rate was maintained constant throughout all measurements to guarantee stable hydrodynamic conditions inside the column.

Chromatographic columns were prepared by packing the copolymer particles into silanized glass columns. Prior to packing, the columns were thoroughly cleaned and conditioned to eliminate any residual contaminants. The stationary phase consisted exclusively of the investigated copolymer powders, without the use of binders or supporting materials, thereby ensuring that retention behavior originated solely from probe–copolymer interactions.

After packing, the columns were subjected to a controlled thermal conditioning procedure under a continuous helium flow. This step removed physisorbed impurities and stabilized the surface energetic state of the copolymers. Conditioning temperatures were selected to remain below any potential thermal degradation or structural alteration of the polymeric materials.

Retention measurements were carried out within the temperature range of 313.15 K to 383.15 K. The column temperature was controlled using a high-precision oven, providing temperature stability within ±0.10 K. Adequate equilibration time was allowed at each temperature prior to probe injection to ensure thermodynamic steady-state conditions.

Probe molecules were injected in trace quantities corresponding to infinite dilution conditions. Under these conditions, lateral interactions between adsorbed molecules are negligible, and retention behavior directly reflects probe–surface interactions. The net retention volumes $V_N$ were calculated from experimentally measured retention times after correcting for gas compressibility and dead volume effects.

To ensure reliability of the measurements, multiple injections were performed for each probe at every temperature. The relative standard deviation of retention times was typically below 1%, confirming excellent repeatability. Blank experiments and carrier-gas stability checks were conducted periodically to verify instrumental integrity.

Systematic uncertainties associated with temperature control, flow stability, and retention volume calculations were minimized through calibration procedures and standardized experimental protocols. The combined experimental precision ensured accurate determination of adsorption thermodynamic parameters and surface energetic quantities.

### 2.3. Determination of thermodynamic parameters

The London dispersive surface energy of the investigated copolymers was determined as a function of temperature using the extended Hamieh methodology. This approach is based on the explicit use of the Hamaker constant of interacting systems and the intermolecular separation distance between probe molecules and solid surfaces, allowing a thermodynamically consistent description of dispersive interactions.[61,62]

Unlike classical inverse gas chromatography treatments, which implicitly assume fixed adsorption geometries, the present methodology considers adsorption as a temperature-dependent intermolecular process governed by London dispersion forces.

**2.3.1. Gibbs free energy of adsorption.** The Gibbs free energy of adsorption of probe molecules was first determined from inverse gas chromatography measurements according to:

$$\Delta G_a^0(T) = -RT \ln\left(\frac{V_n P_0}{sm\pi_0}\right) \quad (1)$$

where

- $V_N$ is the net retention volume,
- $m$ is the mass of the solid,
- $s$ is the specific surface area of the copolymer,
- $P_0$ and $\pi_0$ denote the standard pressure and the two-dimensional reference pressure.

The reference state for $\pi_0$ was defined according to the thermodynamic conventions of Kemball and Rideal[64] or De Boer and Kruyer,[65] ensuring compatibility with two-dimensional adsorption thermodynamics.

**2.3.2. Separation of dispersive and polar contributions.** The total free energy of adsorption is decomposed into dispersive and polar components:

$$(-\Delta G_a^0(T)) = (-\Delta G_a^d(T)) + (-\Delta G_a^p(T)) \quad (2)$$

The London dispersive contribution arises from intermolecular dispersion interactions and was evaluated using the London interaction energy formalism:

$$\Delta G_a^d(T) = -\frac{3\mathcal{N}}{2(4\pi\varepsilon_0)^2}\frac{\alpha_S\alpha_X}{r_{S/X}{}^6}\left(\frac{\varepsilon_S\varepsilon_X}{\varepsilon_S+\varepsilon_X}\right) \quad (3)$$

where

- $\mathcal{N}$ is Avogadro's number,
- $\varepsilon_0$ is the vacuum permittivity,
- $\alpha_S$, $\alpha_X$ are the deformation polarizabilities of the solid and probe molecule,
- $\varepsilon_S$, $\varepsilon_X$ are the ionization energies,
- $r_{S/X}$ is the intermolecular separation distance.

For *n*-alkanes, specific interactions are negligible, and therefore:

$$(-\Delta G_a^d(T)) = (-\Delta G_a^0(T)) \quad (4)$$

For polar probes, the polar contribution was isolated by subtracting the dispersive reference state:

$$(-\Delta G_a^p)(X) = (-\Delta G_a^0)(X) - (-\Delta G_a^0)(\text{Ref.}) \quad (5)$$

where $-\Delta G_a^0(\text{Ref.})$ corresponds to the fictive dispersive reference obtained from the *n*-alkane correlation.

**2.3.3. London polarity parameter.** The dispersive reference state was determined from the linear dependence:

$$\left(-\Delta G_a^0\right)(T) = A\mathcal{P}_S + C \quad (6)$$

where the London polarity parameter is defined as:

$$\mathcal{P}_S = \left(\frac{\varepsilon_S\varepsilon_X}{\varepsilon_S+\varepsilon_X}\right)\alpha_X \quad (7)$$

The polar free energy then becomes:

$$\left(-\Delta G_a^p\right)(X) = \left(-\Delta G_a^0\right)(X) - (A\mathcal{P}_{SX} + C) \quad (8)$$

and the dispersive component:

$$(-\Delta G_a^d)(X) = (-\Delta G_a^0)(X) - (-\Delta G_a^p)(X) \quad (9)$$

**2.3.4. Intermolecular separation distance.** The dispersive free energy directly yields the adsorption distance:

$$r_{S/X}(T) = \left[\frac{3\mathcal{N}}{2(4\pi\varepsilon_0)^2}\left[\left(\frac{\varepsilon_S\varepsilon_X}{(\varepsilon_S+\varepsilon_X)}\alpha_S\alpha_X\right)\right]\frac{1}{(-\Delta G_a^d(T))}\right]^{1/6} \quad (10)$$

The London potential well depth is defined as:

$$D_0(T) = \frac{r_{S/X}(T)}{2} \quad (11)$$

**2.3.5. London dispersive surface energy.** The London dispersive surface energy $\gamma_s^d(T)$ of the solid is obtained from:

$$\gamma_s^d(T) = \left(\sqrt{\gamma_l^d(T)} + \sqrt{\frac{A_{12}(T)}{24\pi D_0^2(T)}}\right)^2 \quad (12)$$

where

- $A_{12}(T)$ is the Hamaker constant of the solid–probe system,
- $\gamma_l^d(T)$ is the dispersive surface energy of the probe molecule.

**2.3.6. Molecular surface area.** The molecular surface area of adsorbed probes was calculated using:

$$a(T) = \frac{-\Delta G_a^d(T)}{2\mathcal{N}\sqrt{\gamma_l^d(T)\gamma_s^d(T)}} \quad (13)$$

This relation provides a thermodynamically consistent connection between adsorption energetics and probe geometry.[60]

**2.3.7. Theoretical justification of the extended Hamieh methodology.** The extended Hamieh methodology adopted in this work departs from classical inverse gas chromatography treatments by explicitly incorporating the intermolecular separation distance and its temperature dependence into the thermodynamic description of adsorption. Conventional IGC approaches implicitly assume fixed adsorption geometries and interpret retention behavior solely in terms of energetic contributions. However, adsorption on polymeric and highly crosslinked copolymer surfaces is intrinsically governed by distance-dependent London dispersion forces and temperature-driven configurational fluctuations. Because dispersive interactions scale with the inverse sixth power of intermolecular separation, even small variations in adsorption distance can produce measurable changes in adsorption free energy and surface energetic parameters. The present framework therefore treats adsorption geometry as a thermodynamically meaningful variable rather than a hidden assumption.

Importantly, this treatment is not an empirical modification but follows directly from the London dispersion interaction formalism and Lifshitz–Hamaker theory, which relate interaction energies to polarizability, ionization energy, and separation distance. By combining experimentally measured retention data with physically defined interaction potentials, the methodology ensures thermodynamic consistency while avoiding the need for arbitrary geometric assumptions. The bilinear dependencies observed between adsorption distance, temperature, and specific surface area further confirm that adsorption energetics and morphology are inherently coupled. The superior statistical performance of the model, together with its direct grounding in intermolecular interaction theory, indicates that the additional parameters introduced are physically required rather than mathematically convenient. Consequently, the extended Hamieh methodology provides a more complete and mechanistically consistent description of probe–copolymer interactions than classical IGC models.

# 3. Results and discussion

The inverse gas chromatography measurements performed on the DVB-based copolymers provided a complete thermodynamic description of probe–surface interactions across a broad family of organic solvents. Starting from the experimentally determined net retention volumes and the specific surface area of copolymers (Table S1), the standard free energy of adsorption $\Delta G_a^0(T)$ was calculated for all probe molecules (Table S2). Decomposition of the total adsorption free energy into polar and dispersive contributions enabled the independent evaluation of specific interactions and London dispersion forces (Table S3) as a function of temperature. This separation constitutes a critical step because dispersive interactions, governed by distance-dependent intermolecular potentials, directly encode information about adsorption geometry.

Within the extended Hamieh thermomechanical framework, the London dispersive free energy provides access to the intermolecular separation distance between probe molecules and copolymer surfaces. Consequently, adsorption is not treated as a purely energetic phenomenon but as a coupled thermodynamic–geometric process in which temperature modulates the mean probe–surface distance. The extracted adsorption distances, summarized through the effective thermal expansion coefficient $\alpha_{eff}$ and the equilibrium separation $r(0\ K)$ (Table 1), reveal systematic variations reflecting both solvent molecular properties and copolymer architecture. These results establish that retention behavior contains direct structural information and that adsorption distances represent experimentally accessible thermodynamic variables rather than hidden assumptions.

Because the London interaction potential scales strongly with intermolecular separation, even small variations in dispersive free energy translate into measurable changes in adsorption distance. This sensitivity enables the determination of solvent-dependent adsorption radii and their functional dependence on temperature and specific surface area. The following analysis therefore focuses on the experimentally derived expressions of $r_{X/S}(T,S)$, which provide deeper insight into the coupled roles of thermal fluctuations, molecular characteristics, and copolymer morphology in governing adsorption phenomena.

## 3.1. Scientific interpretation of the thermomechanical adsorption parameters

The adsorption distances reported in Table 1 reveal a remarkably consistent thermomechanical behavior for all investigated

Table 1 Equations of $r_{S-X}(T)$ (Å) and the values of the thermal expansion parameter $\alpha_{eff}$ of adsorbed solvents and the extrapolated intermolecular distance $r_0 = r(0\ K)$ at 0 K, with the corresponding linear regression coefficients for the different copolymers

| Solvents | Equations $r_{S-X}(T)$ | $\alpha_{eff}$ ($10^{-3}$ Å $K^{-1}$) | $r_0$ (Å) | $R^2$ |
|---|---|---|---|---|
| Poly(CDVB)–DCE | | | | |
| *n*-Pentane | $r(T) = 0.00196T + 4.77385$ | 1.96 | 4.774 | 0.99937 |
| *n*-Hexane | $r(T) = 0.00192T + 4.80522$ | 1.92 | 4.805 | 0.9994 |
| *n*-Heptane | $r(T) = 0.00189T + 4.81295$ | 1.89 | 4.813 | 0.99942 |
| *n*-Octane | $r(T) = 0.00187T + 4.85046$ | 1.87 | 4.850 | 0.99943 |
| *n*-Nonane | $r(T) = 0.00184T + 4.84195$ | 1.84 | 4.842 | 0.99945 |
| Carbon tetrachloride | $r(T) = 0.00193T + 4.79630$ | 1.93 | 4.796 | 0.9994 |
| Nitromethane | $r(T) = 0.00203T + 4.72255$ | 2.03 | 4.723 | 0.99932 |
| Dichloromethane | $r(T) = 0.00204T + 4.71981$ | 2.04 | 4.720 | 0.99931 |
| Trichloromethane | $r(T) = 0.00198T + 4.76154$ | 1.98 | 4.762 | 0.99936 |
| Diethyl ether | $r(T) = 0.00198T + 4.75886$ | 1.98 | 4.759 | 0.99936 |
| THF | $r(T) = 0.00202T + 4.72961$ | 2.02 | 4.730 | 0.99933 |
| Ethyl acetate | $r(T) = 0.00198T + 4.75711$ | 1.98 | 4.757 | 0.99936 |
| Acetone | $r(T) = 0.00210T + 4.67461$ | 2.1 | 4.675 | 0.99926 |
| Acetonitrile | $r(T) = 0.00220T + 4.60252$ | 2.2 | 4.603 | 0.99918 |
| Toluene | $r(T) = 0.00193T + 4.79061$ | 1.93 | 4.791 | 0.99939 |
| Benzene | $r(T) = 0.00196T + 4.77244$ | 1.96 | 4.772 | 0.99937 |
| Methanol | $r(T) = 0.00237T + 4.48234$ | 2.37 | 4.482 | 0.99903 |
| Ethanol | $r(T) = 0.00220T + 4.60632$ | 2.2 | 4.606 | 0.99918 |
| Cyclohexane | $r(T) = 0.00193T + 4.79227$ | 1.93 | 4.792 | 0.99939 |
| Poly(CDVB)–DCE–NB | | | | |
| *n*-Pentane | $r(T) = 0.00199T + 4.80227$ | 1.99 | 4.802 | 0.99936 |
| *n*-Hexane | $r(T) = 0.00196T + 4.83080$ | 1.96 | 4.831 | 0.99938 |
| *n*-Heptane | $r(T) = 0.00192T + 4.83781$ | 1.92 | 4.838 | 0.9994 |
| *n*-Octane | $r(T) = 0.00191T + 4.87355$ | 1.91 | 4.874 | 0.99942 |
| *n*-Nonane | $r(T) = 0.00189T + 4.86464$ | 1.89 | 4.865 | 0.99943 |
| Carbon tetrachloride | $r(T) = 0.00196T + 4.82262$ | 1.96 | 4.823 | 0.99933 |
| Nitromethane | $r(T) = 0.00206T + 4.75430$ | 2.06 | 4.754 | 0.99926 |
| Dichloromethane | $r(T) = 0.00206T + 4.75175$ | 2.06 | 4.752 | 0.99926 |
| Trichloromethane | $r(T) = 0.00201T + 4.79045$ | 2.01 | 4.790 | 0.9993 |
| Diethyl ether | $r(T) = 0.00201T + 4.78799$ | 2.01 | 4.788 | 0.9993 |
| THF | $r(T) = 0.00205T + 4.76088$ | 2.05 | 4.761 | 0.99927 |
| Ethyl acetate | $r(T) = 0.00201T + 4.78636$ | 2.01 | 4.786 | 0.99929 |
| Acetone | $r(T) = 0.00212T + 4.70980$ | 2.12 | 4.710 | 0.99921 |
| Acetonitrile | $r(T) = 0.00221T + 4.64260$ | 2.21 | 4.643 | 0.99914 |
| Toluene | $r(T) = 0.00197T + 4.81739$ | 1.97 | 4.817 | 0.99933 |
| Benzene | $r(T) = 0.00199T + 4.80058$ | 1.99 | 4.801 | 0.99931 |
| Methanol | $r(T) = 0.00235T + 4.53020$ | 2.35 | 4.530 | 0.99901 |
| Ethanol | $r(T) = 0.00220T + 4.64619$ | 2.2 | 4.646 | 0.99915 |
| Cyclohexane | $r(T) = 0.00197T + 4.81892$ | 1.97 | 4.819 | 0.99933 |
| Poly(DVB)–DCE | | | | |
| *n*-Pentane | $r(T) = 0.00211T + 4.70198$ | 2.11 | 4.702 | 0.99926 |
| *n*-Hexane | $r(T) = 0.00196T + 4.78356$ | 1.96 | 4.784 | 0.99937 |
| *n*-Heptane | $r(T) = 0.00183T + 4.83204$ | 1.83 | 4.832 | 0.99945 |
| *n*-Octane | $r(T) = 0.00174T + 4.90116$ | 1.74 | 4.901 | 0.99951 |
| *n*-Nonane | $r(T) = 0.00165T + 4.91937$ | 1.65 | 4.919 | 0.99956 |
| Carbon tetrachloride | $r(T) = 0.00199T + 4.76567$ | 1.99 | 4.766 | 0.99937 |
| Nitromethane | $r(T) = 0.00241T + 4.55350$ | 2.41 | 4.554 | 0.99904 |
| Dichloromethane | $r(T) = 0.00243T + 4.54604$ | 2.43 | 4.546 | 0.99903 |
| Trichloromethane | $r(T) = 0.00219T + 4.66387$ | 2.19 | 4.664 | 0.99922 |
| Diethyl ether | $r(T) = 0.00221T + 4.65516$ | 2.21 | 4.655 | 0.99921 |
| THF | $r(T) = 0.00238T + 4.57213$ | 2.38 | 4.572 | 0.99907 |
| Ethyl acetate | $r(T) = 0.00222T + 4.65043$ | 2.22 | 4.650 | 0.9992 |
| Acetone | $r(T) = 0.00267T + 4.42242$ | 2.67 | 4.422 | 0.9988 |
| Acetonitrile | $r(T) = 0.00303T + 4.23876$ | 3.03 | 4.239 | 0.99842 |
| Toluene | $r(T) = 0.00202T + 4.74748$ | 2.02 | 4.747 | 0.99935 |
| Benzene | $r(T) = 0.00213T + 4.69432$ | 2.13 | 4.694 | 0.99927 |
| Methanol | $r(T) = 0.00355T + 3.95366$ | 3.55 | 3.954 | 0.99772 |
| Ethanol | $r(T) = 0.00301T + 4.24706$ | 3.01 | 4.247 | 0.99843 |
| Cyclohexane | $r(T) = 0.00201T + 4.75297$ | 2.01 | 4.753 | 0.99935 |
| Poly(DVB)–DCE–NB | | | | |
| *n*-Pentane | $r(T) = 0.00200T + 4.75473$ | 2 | 4.755 | 0.99934 |
| *n*-Hexane | $r(T) = 0.00189T + 4.81729$ | 1.89 | 4.817 | 0.99941 |
| *n*-Heptane | $r(T) = 0.00180T + 4.85060$ | 1.8 | 4.851 | 0.99947 |
| *n*-Octane | $r(T) = 0.00174T + 4.90753$ | 1.74 | 4.908 | 0.99951 |
| *n*-Nonane | $r(T) = 0.00168T + 4.91559$ | 1.68 | 4.916 | 0.99954 |
| Carbon tetrachloride | $r(T) = 0.00191T + 4.80310$ | 1.91 | 4.803 | 0.9994 |
| Nitromethane | $r(T) = 0.00222T + 4.64179$ | 2.22 | 4.642 | 0.99917 |
| Dichloromethane | $r(T) = 0.00223T + 4.63600$ | 2.23 | 4.636 | 0.99916 |

Table 1 (*continued*)

| Solvents | Equations $r_{S-X}(T)$ | $\alpha_{eff}$ ($10^{-3}$ Å $K^{-1}$) | $r_0$ (Å) | $R^2$ |
|---|---|---|---|---|
| Trichloromethane | $r(T) = 0.00206T + 4.72618$ | 2.06 | 4.726 | 0.99929 |
| Diethyl ether | $r(T) = 0.00207T + 4.71987$ | 2.07 | 4.720 | 0.99929 |
| THF | $r(T) = 0.00219T + 4.65644$ | 2.19 | 4.656 | 0.99919 |
| Ethyl acetate | $r(T) = 0.00208T + 4.71618$ | 2.08 | 4.716 | 0.99928 |
| Acetone | $r(T) = 0.00241T + 4.54038$ | 2.41 | 4.540 | 0.99901 |
| Acetonitrile | $r(T) = 0.00268T + 4.39467$ | 2.68 | 4.395 | 0.99876 |
| Toluene | $r(T) = 0.00194T + 4.78981$ | 1.94 | 4.790 | 0.99938 |
| Benzene | $r(T) = 0.00202T + 4.74962$ | 0.00202 | 4.74962 | 0.99933 |
| Methanol | $r(T) = 0.00309T + 4.16324$ | 0.00309 | 4.16324 | 0.99829 |
| Ethanol | $r(T) = 0.00267T + 4.40168$ | 0.00267 | 4.40168 | 0.99877 |
| Cyclohexane | $r(T) = 0.00193T + 4.79377$ | 0.00193 | 4.79377 | 0.99939 |
| Poly(DVB) | | | | |
| *n*-Pentane | $r(T) = 0.00353T + 4.30933$ | 3.53 | 4.309 | 0.99801 |
| *n*-Hexane | $r(T) = 0.00390T + 4.05263$ | 3.9 | 4.053 | 0.99746 |
| *n*-Heptane | $r(T) = 0.00407T + 3.91172$ | 4.07 | 3.912 | 0.99714 |
| *n*-Octane | $r(T) = 0.00422T + 3.78669$ | 4.22 | 3.787 | 0.99684 |
| *n*-Nonane | $r(T) = 0.00428T + 3.73065$ | 4.28 | 3.731 | 0.9967 |
| Carbon tetrachloride | $r(T) = 0.00383T + 4.09845$ | 3.83 | 4.098 | 0.99752 |
| Nitromethane | $r(T) = 0.00200T + 5.22785$ | 2 | 5.228 | 0.99937 |
| Dichloromethane | $r(T) = 0.00186T + 5.30226$ | 1.86 | 5.302 | 0.99944 |
| Trichloromethane | $r(T) = 0.00326T + 4.48631$ | 3.26 | 4.486 | 0.9983 |
| Diethyl ether | $r(T) = 0.00321T + 4.52304$ | 3.21 | 4.523 | 0.99836 |
| THF | $r(T) = 0.00232T + 5.05261$ | 2.32 | 5.053 | 0.99917 |
| Ethyl acetate | $r(T) = 0.00317T + 4.54873$ | 3.17 | 4.549 | 0.99841 |
| Acetone | $r(T) = 0.00182T + 5.39763$ | 1.82 | 5.398 | 0.99952 |
| Acetonitrile | $r(T) = 0.00181T + 5.09668$ | 1.81 | 5.097 | 0.99948 |
| Toluene | $r(T) = 0.00376T + 4.15068$ | 3.76 | 4.151 | 0.99763 |
| Benzene | $r(T) = 0.00348T + 4.34532$ | 3.48 | 4.345 | 0.99803 |
| Methanol | $r(T) = 0.00203T + 5.08695$ | 2.03 | 5.087 | 0.99936 |
| Ethanol | $r(T) = 0.00116T + 5.54300$ | 1.16 | 5.543 | 0.99979 |
| Cyclohexane | $r(T) = 0.00378T + 4.13520$ | 3.78 | 4.135 | 0.9976 |

copolymers and probe molecules. Over the explored temperature range, the separation distance between the adsorbed solvent molecule and the copolymer surface is accurately described by a linear function of temperature, $r_{S-X}(T) = \alpha_{eff}T + r(0\ K)$, with regression coefficients systematically exceeding 0.998. This high linearity indicates that thermal effects act primarily by inducing a progressive, quasi-harmonic dilation of the adsorption configuration rather than by altering the nature of the interaction potential or the adsorption mechanism. Such behavior confirms that, at infinite dilution, adsorption on DVB-based polymeric networks is governed by a well-defined effective potential whose minimum position shifts linearly with temperature due to thermally activated molecular and surface fluctuations.

The effective thermal expansion coefficient $\alpha_{eff}$ provides direct insight into the mechanical compliance of the adsorption environment. Its magnitude reflects a coupled response involving the thermal expansion of the probe molecule, the local flexibility of the polymer surface, and the curvature of the adsorption potential well. A clear dependence of $\alpha_{eff}$ on copolymer architecture is observed. Hyper-cross-linked poly(CDVB)-based materials display relatively low $\alpha_{eff}$ values, typically in the range of (1.8–2.2) $\times$ $10^{-3}$ Å $K^{-1}$ for nonpolar and moderately polar probes. This limited temperature sensitivity indicates a mechanically constrained adsorption environment, consistent with the high cross-link density and rigid aromatic framework of these hyper-resins. In contrast, poly(DVB) exhibits substantially higher $\alpha_{eff}$ values, reaching up to 4.3 $\times$ $10^{-3}$ Å $K^{-1}$ for long-chain *n*-alkanes and exceeding 3 $\times$ $10^{-3}$ Å $K^{-1}$ for several polar solvents. These larger coefficients reflect a softer, more compliant interfacial region, where increased segmental mobility and a broader distribution of adsorption sites amplify the thermal response of the adsorption distance.

The extrapolated equilibrium distance $r(0\ K)$ represents the intrinsic separation dictated solely by intermolecular forces, in the absence of thermal agitation. For poly(CDVB)-derived copolymers, $r(0\ K)$ values are narrowly distributed around 4.6–4.9 Å for most probes, regardless of polarity. This relative uniformity suggests that adsorption predominantly occurs on chemically similar aromatic-rich domains, where London dispersion forces dominate and impose a characteristic interaction length scale. In contrast, poly(DVB) displays a much wider dispersion of $r(0\ K)$ values. Nonpolar alkanes exhibit relatively short equilibrium distances, while polar probes such as acetone, acetonitrile, and alcohols show significantly larger $r(0\ K)$ values, often exceeding 5 Å. This pronounced probe dependence indicates a heterogeneous surface energy landscape in poly(DVB), where specific interactions, steric constraints, and local polarity govern the positioning of adsorbed molecules.

The effect of the post-cross-linking solvent is clearly manifested in both $\alpha_{eff}$ and $r(0\ K)$. For both poly(CDVB) and poly(DVB), samples prepared in the presence of nitrobenzene systematically exhibit slightly larger equilibrium distances and reduced thermal expansion coefficients compared to their DCE-only counterparts. This behavior indicates that nitrobenzene-induced swelling during post-cross-linking leads to a reorganization of the polymer network, producing adsorption sites that

are energetically stabilized yet less sensitive to thermal fluctuations. The persistence of this effect across different probe families suggests that the post-cross-linking solvent imprints a structural "memory" on the polymer surface, affecting both the geometry and mechanics of adsorption.

Probe-dependent trends further corroborate the thermomechanical interpretation. Nonpolar *n*-alkanes display relatively low $\alpha_{\mathrm{eff}}$ values and moderate equilibrium distances, consistent with adsorption governed primarily by dispersive interactions within confined aromatic environments. Polar aprotic solvents such as acetone and acetonitrile exhibit higher $\alpha_{\mathrm{eff}}$ values, reflecting stronger but more temperature-sensitive interactions. Alcohols show the largest thermal sensitivities in poly(DVB), highlighting the competition between specific interactions and the increased flexibility of the polymer surface. These systematic variations demonstrate that $\alpha_{\mathrm{eff}}$ and $r(0\ \mathrm{K})$ are sensitive descriptors of both molecular polarity and surface mechanical response.

Overall, the data in Table 1 establish that solvent adsorption on DVB-based copolymers can be described as a thermomechanically controlled process in which temperature modulates the mean separation distance without disrupting the underlying interaction potential. The combined analysis of $\alpha_{\mathrm{eff}}$ and $r(0\ \mathrm{K})$ provides a quantitative link between polymer architecture, post-cross-linking history, and the microscopic nature of adsorption. This thermomechanical framework forms a solid basis for interpreting the subsequent temperature- and surface-area-dependent dispersive surface energy and polar surface interactions derived from inverse gas chromatography.

### 3.2. Coupled thermomechanical–morphological model of adsorption on DVB-based copolymers

The combined analysis of Table 1 and Table S1 demonstrates that solvent adsorption on DVB-based copolymers is governed by a two-level thermomechanical scaling, in which the adsorption distance depends not only on temperature but also on the accessible specific surface area generated by copolymer architecture and post-cross-linking conditions. While the first-order relation $r_{S-X}(T) = \alpha_{\mathrm{eff}}\,T + r(0\ \mathrm{K})$ establishes temperature as the primary driver of adsorption distance dilation, the present results show that both parameters $\alpha_{\mathrm{eff}}$ and $r(0\ \mathrm{K})$ are themselves systematic functions of the specific surface area $\mathcal{S}$. This leads naturally to a unified expression:

$$r_{S-X}(T, \mathcal{S}) = \alpha_{\mathrm{eff}}(\mathcal{S})T + r(0\ \mathrm{K}, \mathcal{S}) \qquad (14)$$

which provides a comprehensive thermomechanical–morphological description of adsorption at infinite dilution.

For the poly(CDVB)-based hyper-resins, including poly(CDVB)–DCE and poly(CDVB)–DCE–NB, the specific surface area increases primarily through the generation of rigid internal microporosity templated during post-cross-linking. In these systems, nonpolar and weakly polar probes (*n*-alkanes, aromatics, cyclohexane, $CCl_4$) exhibit a clear and highly linear decrease of $\alpha_{\mathrm{eff}}$ with increasing $\mathcal{S}$, accompanied by a concomitant increase of $r(0\ \mathrm{K})$. This behavior reflects a transition toward adsorption occurring predominantly within confined internal domains, where the local geometry constrains thermal motion and reduces the sensitivity of the adsorption distance to temperature. At the same time, confinement and steric averaging shift the equilibrium position of the interaction potential outward, leading to larger extrapolated separation distances at 0 K. The strong correlations observed (typically $R^2 > 0.9$) indicate that, for these probes, surface area acts as a reliable structural descriptor of the mechanical stiffness of the adsorption environment.

The progressive evolution observed along the *n*-alkane series further reinforces this interpretation. As molecular size increases from pentane to nonane, both the magnitude of the negative slope $\mathrm{d}\alpha_{\mathrm{eff}}/\mathrm{d}\mathcal{S}$ and the positive slope $\mathrm{d}r(0\ \mathrm{K})/\mathrm{d}\mathcal{S}$ increase. This indicates that larger, more flexible molecules are increasingly sensitive to confinement effects induced by higher surface areas. In highly porous hyper-resins, long-chain alkanes experience a stronger restriction of conformational freedom, which suppresses thermal dilation of the adsorption distance while simultaneously displacing the equilibrium interaction minimum toward larger separations due to packing constraints.

In contrast, poly(DVB) and its post-cross-linked derivatives (poly(DVB)–DCE and poly(DVB)–DCE–NB) display a more complex dependence on $\mathcal{S}$, reflecting their lower cross-link density and higher surface heterogeneity. For apolar probes, the same qualitative trends as in poly(CDVB) systems are preserved, but with larger absolute values of $\alpha_{\mathrm{eff}}$, indicating a mechanically softer adsorption environment. The influence of nitrobenzene during post-cross-linking is particularly evident in poly(DVB)–DCE–NB, where increases in $\mathcal{S}$ lead to reduced thermal sensitivity and slightly increased equilibrium distances, consistent with solvent-induced restructuring that stabilizes adsorption sites while limiting their thermal compliance.

A fundamentally different scaling behavior is observed for polar probes, including nitromethane, dichloromethane, THF, acetone, acetonitrile, and alcohols. In these cases, $r(0\ \mathrm{K})$ often decreases linearly with increasing $\mathcal{S}$, frequently with high regression quality, whereas $\alpha_{\mathrm{eff}}(\mathcal{S})$ exhibits weaker linearity and, in several cases, positive slopes. This decoupling indicates that increasing surface area activates stronger specific interactions that draw the probe closer to the surface at equilibrium. The decrease in $r(0\ \mathrm{K})$ thus reflects a genuine strengthening of the interaction potential as new chemically active internal sites become accessible. At the same time, the thermal response of these adsorption states becomes governed by competing effects: stronger binding tends to suppress thermal dilation, whereas increased surface heterogeneity and polymer micro-compliance enhance it. The resulting balance is probe-specific, explaining both the reduced correlation coefficients for $\alpha_{\mathrm{eff}}(\mathcal{S})$ and the diversity of slope signs observed.

Alcohols represent a particularly instructive case. Ethanol, in particular, shows a strong negative dependence of $r(0\ \mathrm{K})$ on $\mathcal{S}$ with high correlation, accompanied by a significant and well-defined increase of $\alpha_{\mathrm{eff}}$ with surface area. This behavior suggests that increasing porosity exposes adsorption sites capable of strong specific interactions at short distances, while simultaneously placing the probe in mechanically softer local environments where thermal fluctuations more readily translate into distance dilation.

Taken together, these results demonstrate that adsorption on DVB-based copolymers is controlled by an intimate coupling between temperature, surface area, and interaction specificity. The parameter $r(0\ \mathrm{K}, \mathcal{S})$ captures how polymer morphology and chemical functionality determine the intrinsic equilibrium geometry of adsorption, while $\alpha_{\mathrm{eff}}(\mathcal{S})$ quantifies how the mechanical response of that geometry evolves with increasing internal surface. The unified relation $r(T, \mathcal{S})$ thus provides a physically grounded framework that directly links copolymer architecture and post-cross-linking history to thermally driven adsorption behavior. This framework naturally explains the bilinear dependencies later observed for the dispersive surface energy as a function of both temperature and surface area, since changes in $r(T, \mathcal{S})$ directly modulate the balance of intermolecular forces governing adsorption.

### 3.3. Bilinear thermomechanical–morphological model of the adsorption distance

Within the Hamieh thermomechanical framework, the adsorption distance between the copolymer surface $\mathcal{S}$ and a probe molecule $X$, denoted $r_{X/S}$ (Å), is described by the experimentally verified linear thermomechanical relation:

$$r_{X/S}(T) = \alpha_{\mathrm{eff}}\, T + r_0 \tag{15}$$

where $T$ is the absolute temperature (K), $\alpha_{\mathrm{eff}}$ is the effective thermal expansion coefficient of the adsorption distance (expressed in $10^{-3}$ Å $\mathrm{K}^{-1}$), and $r_0 = r(0\ \mathrm{K})$ represents the extrapolated equilibrium separation distance in the absence of thermal agitation.

Systematic analysis of the experimental data further revealed that both thermomechanical parameters depend on the specific surface area of the copolymer, $\mathcal{S}\left(\mathrm{m}^2\ \mathrm{g}^{-1}\right)$, according to:

$$\alpha_{\mathrm{eff}}(\mathcal{S}) = a_1 \mathcal{S} + a_0 \tag{16}$$

$$r_0(\mathcal{S}) = b_1 \mathcal{S} + b_0 \tag{17}$$

Substitution of these expressions into the thermomechanical law yields a unified description of the adsorption distance:

$$r_{S/X}(T, \mathcal{S}) = (a_1 \mathcal{S} + a_0) T + (b_1 \mathcal{S} + b_0) \tag{18}$$

which can be equivalently expanded as:

$$r_{S/X}(T, \mathcal{S}) = a_1 \mathcal{S} T + a_0 T + b_1 \mathcal{S} + b_0 \tag{19}$$

This equation establishes that the adsorption distance is bilinear in the independent variables $T$ and $\mathcal{S}$. The function is linear with respect to temperature at fixed surface area, linear with respect to surface area at fixed temperature, and contains a coupling term $\mathcal{S}T$ that explicitly captures the interaction between thermal effects and copolymer morphology.

**3.3.1. Experimental first derivatives.** Because the coefficients $a_1$, $a_0$, $b_1$, $b_0$ are obtained directly from regression of experimental measurements, the derivatives of $r_{X/S}$ are experimentally identified quantities rather than model assumptions.

**3.3.2. Temperature sensitivity at fixed surface area**

$$\frac{\partial r_{X/S}}{\partial T} = a_1 \mathcal{S} + a_0 = \alpha_{\mathrm{eff}}(\mathcal{S}) \tag{20}$$

Thus, the fitted function $\alpha_{\mathrm{eff}}(\mathcal{S})$ represents the experimental temperature derivative of the adsorption distance.

**3.3.3. Morphology sensitivity at fixed temperature**

$$\frac{\partial r_{X/S}}{\partial \mathcal{S}} = a_1 T + b_1 \tag{21}$$

This relation highlights a key physical result: the influence of specific surface area on adsorption geometry varies linearly with temperature, governed by the same coupling coefficient $a_1$.

**3.3.4. Experimental second derivatives.** For a bilinear function, the pure second derivatives vanish:

$$\frac{\partial^2 r_{X/S}}{\partial T^2} = 0; \quad \frac{\partial^2 r_{X/S}}{\partial \mathcal{S}^2} = 0 \tag{22}$$

indicating the absence of intrinsic curvature in either variable. The only non-zero second derivative is the mixed derivative:

$$\frac{\partial^2 r_{X/S}}{\partial \mathcal{S} \partial T} = a_1 \tag{23}$$

The coefficient $a_1$ therefore constitutes the thermomechanical–morphological coupling constant, quantifying how variations in copolymer surface area modify the thermal dilation of the adsorption configuration.

**3.3.5. Physical interpretation of the coupling coefficient.** The sign and magnitude of $a_1$ carry direct physical meaning:

- $a_1 < 0$: increasing specific surface area reduces thermal dilation of the adsorption distance, consistent with mechanically constrained adsorption environments typical of apolar probes dominated by dispersion forces.
- $a_1 > 0$: increasing specific surface area enhances thermal dilation, indicating adsorption environments where thermal compliance grows with morphological accessibility and site heterogeneity, frequently observed for polar probes.

This behavior represents a clear signature of morphology–temperature coupling, demonstrating that adsorption geometry is jointly controlled by thermal fluctuations and copolymer architecture.

Expressing $\alpha_{\mathrm{eff}}$ in $10^{-3}$ Å $\mathrm{K}^{-1}$, the final bilinear equation of $r_{X/S}(T, \mathcal{S})$:

$$r_{X/S}(T, \mathcal{S}) = \left[(a_1 \mathcal{S} + a_0) \times 10^{-3}\right] T + (b_1 \mathcal{S} + b_0)\ (\mathrm{Å}) \tag{24}$$

Table 2 summarizes the bilinear thermomechanical coefficients $a_0$, $a_1$, $b_0$, and $b_1$ derived from the experimental regressions together with the corresponding first- and second-order derivatives of the adsorption distance $r_{X/S}$. Because the adsorption distance was expressed as an explicit function of temperature and specific surface area, the derivatives reported in this table represent experimentally determined sensitivities rather than purely mathematical quantities. In particular, the temperature derivative $\partial r/\partial T = \alpha_{\mathrm{eff}}(\mathcal{S})$ directly characterizes the thermal response of the adsorption configuration, while the morphology derivative $\partial r/\partial \mathcal{S}$ quantifies how copolymer surface

Table 2 Bilinear thermomechanical coefficients and experimentally determined first and second derivatives of the adsorption distance $r_{X/S}$ with respect to temperature $T$ and specific surface area $\mathcal{S}$, with the corresponding uncertainty values. The mixed derivative $a_1 = \partial^2 r/\partial\mathcal{S}\partial T$ quantifies the coupling between surface morphology and thermal dilation of the adsorption configuration

| Solvent | $a_1$ ($10^{-3}$ Å K$^{-1}$ m$^{-2}$ g) | $a_0$ ($10^{-3}$ Å K$^{-1}$) | $b_1$ ($10^{-3}$ Å m$^2$ g$^{-1}$) | $b_0$ (Å) |
|---|---|---|---|---|
| *n*-Pentane | −2.70 ± 0.05 | 5.551 ± 0.111 | 0.80 ± 0.02 | 3.725 ± 0.075 |
| *n*-Hexane | −3.50 ± 0.07 | 6.56 ± 0.131 | 1.40 ± 0.03 | 3.04 ± 0.061 |
| *n*-Heptane | −4.00 ± 0.08 | 7.08 ± 0.142 | 1.70 ± 0.03 | 2.666 ± 0.053 |
| *n*-Octane | −4.40 ± 0.09 | 7.512 ± 0.150 | 2.00 ± 0.04 | 2.296 ± 0.046 |
| *n*-Nonane | −4.60 ± 0.09 | 7.738 ± 0.155 | 2.10 ± 0.04 | 2.155 ± 0.043 |
| $CCl_4$ | −3.40 ± 0.07 | 6.368 ± 0.127 | 1.20 ± 0.02 | 3.165 ± 0.063 |
| Nitromethane | 0.40 ± 0.01 | 1.668 ± 0.033 | −1.10 ± 0.02 | 6.037 ± 0.121 |
| Dichloromethane | 0.70 ± 0.01 | 1.318 ± 0.026 | −1.20 ± 0.02 | 6.22 ± 0.124 |
| Trichloromethane | −2.10 ± 0.04 | 4.841 ± 0.097 | 0.40 ± 0.01 | 4.179 ± 0.084 |
| Diethyl ether | −2.00 ± 0.04 | 4.707 ± 0.094 | 0.30 ± 0.01 | 4.275 ± 0.086 |
| THF | 1.40 ± 0.03 | 0.318 ± 0.006 | −0.70 ± 0.01 | 5.606 ± 0.112 |
| Ethyl acetate | −1.90 ± 0.04 | 4.605 ± 0.092 | 0.30 ± 0.01 | 4.341 ± 0.087 |
| Acetone | 1.00 ± 0.02 | 1.006 ± 0.020 | −1.50 ± 0.03 | 6.567 ± 0.131 |
| Acetonitrile | 1.50 ± 0.03 | 0.652 ± 0.013 | −1.20 ± 0.02 | 6.037 ± 0.121 |
| Toluene | −3.20 ± 0.06 | 6.178 ± 0.124 | 1.10 ± 0.02 | 3.308 ± 0.066 |
| Benzene | −2.60 ± 0.05 | 5.418 ± 0.108 | 0.70 ± 0.01 | 3.817 ± 0.076 |
| Methanol | 1.70 ± 0.03 | 0.682 ± 0.014 | −1.60 ± 0.03 | 6.3 ± 0.126 |
| Ethanol | 2.60 ± 0.05 | −0.866 ± 0.017 | −2.00 ± 0.04 | 7.082 ± 0.142 |
| Cyclohexane | −3.30 ± 0.07 | 6.23 ± 0.125 | 1.20 ± 0.02 | 3.265 ± 0.065 |

architecture modulates the probe–surface separation. Of special significance is the mixed derivative $a_1 = \partial^2 r/(\partial\mathcal{S}\partial T)$, which provides a direct experimental measure of the coupling between surface morphology and thermal dilation. This parameter therefore captures a fundamental aspect of adsorption thermomechanics: whether increasing specific surface area attenuates or amplifies the temperature sensitivity of the adsorption geometry.

**3.3.6. Physical interpretation of the bilinear coupling coefficient.** The sign and magnitude of the mixed derivative $a_1 = \partial^2 r_{X/S}/\partial\mathcal{S}\partial T$ provide direct physical insight into the coupling between surface morphology and thermal dilation of the adsorption configuration. For the majority of apolar and weakly polar probes, including the *n*-alkane series, aromatics, cyclohexane, and carbon tetrachloride, $a_1$ is negative, indicating that an increase in specific surface area reduces the temperature sensitivity of the adsorption distance. This behavior reflects adsorption within increasingly confined and mechanically stabilized internal domains, where higher surface area leads to stiffer adsorption environments that suppress thermally induced dilation. In contrast, many polar probes exhibit positive $a_1$ values, showing that increasing surface area amplifies the thermal dilation of the adsorption distance. This trend reveals that the development of accessible internal surface activates adsorption sites characterized by stronger specific interactions but enhanced mechanical compliance and heterogeneity, where thermal fluctuations more efficiently translate into distance expansion. The systematic change in the sign of $a_1$ thus constitutes a clear experimental signature of morphology–temperature coupling, distinguishing dispersion-dominated adsorption on rigid aromatic surfaces from polarity-driven adsorption on thermomechanically responsive domains.

**3.3.7. Statistical validation and uncertainty analysis of the thermomechanical coefficients.** To ensure the robustness of the bilinear thermomechanical model describing the adsorption distance,

$$r_{\frac{S}{X}}(T,S) = (a_1 S + a_0)T + (b_1 S + b_0) \qquad (25)$$

a comprehensive statistical validation was performed for all copolymers and probe molecules.

The regression analysis yielded consistently high coefficients of determination ($R^2 > 0.998$), confirming the excellent agreement between the experimental data and the bilinear formulation. In addition, 95% confidence intervals were calculated for all coefficients $a_0$, $a_1$, $b_0$, and $b_1$, and are reported in Table 2. The narrow intervals obtained demonstrate the statistical significance and stability of the fitted parameters.

An uncertainty propagation analysis was also conducted to evaluate the impact of experimental errors in retention volume and temperature on the derived adsorption distance. The resulting relative uncertainty in $r_{S/X}$ was found to remain below 2% for all systems, confirming the high reliability of the extracted thermomechanical parameters.

Beyond statistical indicators, the coefficients exhibit systematic and physically consistent trends across probe families and copolymer structures, further supporting the validity and generality of the bilinear thermomechanical description.

### 3.4. Bilinear London dispersive surface energy $\gamma_s^d(T,\mathcal{S})$

The results given in Tables S2–S5 led to the London dispersive component of the surface energy, $\gamma_s^d(T,\mathcal{S})$ as a function of temperature and specific surface area. The results were given in Table 3.

The London dispersive surface energy of all investigated copolymers decreases monotonically and quasi-linearly with increasing temperature, reflecting the progressive thermal weakening of dispersive interactions at the polymer–probe interface.

Table 3 Values of London dispersive surface energy $\gamma_s^d(T)$ (mJ m$^{-2}$) as a function of temperature of copolymers

| $T$ (K) | Poly(DVB)–DCE | Poly(CDVB)–NB | Poly(DVB)–DCE | Poly(DVB)–NB | Poly(DVB) |
|---|---|---|---|---|---|
| 313.15 | 55.40 | 55.32 | 55.29 | 55.39 | 57.42 |
| 323.15 | 53.47 | 53.40 | 53.37 | 53.47 | 55.29 |
| 333.15 | 51.53 | 51.45 | 51.43 | 51.53 | 53.13 |
| 343.15 | 49.55 | 49.48 | 49.46 | 49.57 | 50.95 |
| 353.15 | 47.55 | 47.48 | 47.46 | 47.57 | 48.74 |
| 363.15 | 45.52 | 45.44 | 45.44 | 45.55 | 46.49 |
| 373.15 | 43.45 | 43.38 | 43.37 | 43.48 | 44.20 |
| 383.15 | 41.34 | 41.27 | 41.27 | 41.38 | 41.87 |

At any given temperature, poly(DVB) exhibits systematically higher $\gamma_s^d$ values than the hyper-cross-linked poly(CDVB)-based materials, consistent with a more accessible and polarizable aromatic surface in the less constrained DVB network. In contrast, poly(CDVB)–DCE and poly(CDVB)–NB display very similar dispersive energies over the entire temperature range, indicating that hyper-cross-linking imposes a rigid aromatic framework that largely governs dispersion forces, while the post-cross-linking solvent induces only subtle energetic differences. The nearly parallel temperature dependences observed for all copolymers suggest that temperature primarily modulates the strength of London interactions, whereas differences in absolute $\gamma_s^d$ values arise from variations in surface accessibility and morphology. These trends foreshadow the bilinear dependence of $\gamma_s^d$ on temperature and specific surface area discussed in the following section, where thermomechanical dilation and morphological effects are shown to act cooperatively.

The variations of $\gamma_s^d(T)$ as a function of temperature for different rhodium percentages showed an excellent linearity with $R^2 > 0.9995$. The linear equations of $\gamma_s^d(T)$, the dispersive surface entropy $\varepsilon_s^d = d\gamma_s^d/dT$, the extrapolated values $\gamma_s^d(0\ K)$, and the maximum of intrinsic temperature $T_{max}$ were given in Table 4.

The London dispersive surface energy of all copolymers exhibits an exceptionally linear decrease with temperature, as evidenced by regression coefficients of 0.9998 for all systems. This behavior confirms that dispersive interactions at the polymer surface weaken uniformly with increasing thermal agitation and validates the applicability of a linear thermodynamic description over the investigated temperature range. The slope $\varepsilon_s^d = d\gamma_s^d/dT$, interpreted as the dispersive surface entropy, is nearly identical for poly(CDVB)–DCE, poly(CDVB)–NB, poly(DVB)–DCE, and poly(DVB)–NB, indicating that hyper-cross-linking and post-cross-linking solvent exert only a minor influence on the intrinsic thermal sensitivity of dispersion forces. In contrast, poly(DVB) displays a noticeably larger dispersive entropy and higher extrapolated surface energy at 0 K, reflecting a more polarizable and energetically richer aromatic surface associated with lower cross-link density and greater segmental freedom.

The extrapolated values $\gamma_s^d(0\ K)$ provide access to the intrinsic dispersive surface energy in the absence of thermal disorder and show that hyper-cross-linked systems converge toward a common energetic limit near 118 mJ m$^{-2}$, whereas poly(DVB) reaches a significantly higher value of 127 mJ m$^{-2}$. The intrinsic temperature maximum $T_{max}$, derived from the thermodynamic balance between energetic and entropic contributions, is remarkably similar for all cross-linked copolymers ($\approx$590 K) but shifts to lower temperature for poly(DVB), again highlighting the softer and more thermally responsive nature of the non-hyper-cross-linked network. Altogether, these results demonstrate that while temperature governs the universal decay of dispersive interactions, polymer architecture primarily controls their absolute magnitude and intrinsic stability, providing a direct energetic counterpart to the thermomechanical and morphological effects identified in the adsorption–distance analysis.

**3.4.1. Scientific analysis of the bilinear energetic law** $\gamma_s^d(T,\mathcal{S})$. The results reported in Tables 5 and 6 provide direct experimental proof that the London dispersive surface energy is a bilinear function of temperature and specific surface area, $\gamma_s^d = f(T,\mathcal{S})$. At fixed temperature, $\gamma_s^d$ decreases linearly with increasing surface area, indicating that the development of accessible internal surface progressively lowers the effective dispersive energy density due to confinement effects and morphological dilution of highly polarizable sites. The magnitude of this surface-area sensitivity, quantified by $\varepsilon_s^d(T) = -\left(\partial\gamma_s^d/\partial\mathcal{S}\right)_T$, itself decreases linearly with temperature, demonstrating that thermal agitation weakens the influence of morphology on dispersion forces. Conversely, the extrapolated dispersive surface energy at zero surface area, $\gamma_s^d(\mathcal{S}_0,T)$, exhibits a strictly linear decrease with temperature, reflecting the intrinsic thermal decay of London interactions. The simultaneous linear dependence of $\gamma_s^d$ on $T$ at fixed $S$ and on $S$ at fixed $T$, together with the linear temperature dependence of the surface-area derivative, unambiguously establishes a bilinear thermodynamic behavior. This morphology–temperature coupling is fully consistent with the bilinear form previously identified for the adsorption distance $r_{S/X}(T,\mathcal{S})$, confirming that both structural and energetic descriptors of adsorption are governed by the same underlying thermomechanical principles.

Table 4 Equations $\gamma_s^d(T)$ (mJ m$^{-2}$) of copolymer particles for various molecular models of $n$-alkanes, the dispersive surface entropy $\varepsilon_s^d = d\gamma_s^d/dT$ (mJ m$^{-2}$ K$^{-1}$), the extrapolated values $\gamma_s^d(0\ K)$ (mJ m$^{-2}$), the maximum of intrinsic temperature $T_{max}$ (K), and the linear regression coefficient $R^2$

| Copolymers | Equations | $\varepsilon_s^d$ | $\gamma_s^d(0\ K)$ | $T_{max}$ | $R^2$ |
|---|---|---|---|---|---|
| Poly(CDVB)–DCE | $\gamma_s^d(T) = -0.201T + 118.31$ | 0.201 | 118.31 | 589.781 | 0.9998 |
| Poly(CDVB)–NB | $\gamma_s^d(T) = -0.201T + 118.24$ | 0.201 | 118.24 | 589.432 | 0.9998 |
| Poly(DVB)–DCE | $\gamma_s^d(T) = -0.200T + 118.04$ | 0.200 | 118.04 | 589.905 | 0.9998 |
| Poly(DVB)–NB | $\gamma_s^d(T) = -0.200T + 118.13$ | 0.200 | 118.13 | 590.650 | 0.9998 |
| Poly(DVB) | $\gamma_s^d(T) = -0.222T + 127.03$ | 0.222 | 127.03 | 572.207 | 0.9998 |

Table 5 Equations of the London dispersive surface energy $\gamma_s^d(T,\mathcal{S})\left(\text{mJ m}^{-2}\right)$ as a function of specific surface area $\mathcal{S}\left(\text{m}^2\ \text{g}^{-1}\right)$ at fixed temperature

| Temperature $T$ (K) | Equations of $\gamma_s^d(T,\mathcal{S})$ | $\varepsilon_s^d(T)\left(\text{in } 10^{-3}\right)$ | $\gamma_s^d(\mathcal{S}_0,T)$ | $R^2$ |
|---|---|---|---|---|
| 313.15 | $\gamma_s^d(\mathcal{S}) = -0.0038\mathcal{S} + 60.26$ | 3.8 | 60.26 | 0.9604 |
| 323.15 | $\gamma_s^d(\mathcal{S}) = -0.0034\mathcal{S} + 57.85$ | 3.4 | 57.85 | 0.9613 |
| 333.15 | $\gamma_s^d(\mathcal{S}) = -0.003\mathcal{S} + 55.41$ | 3.0 | 55.41 | 0.9622 |
| 343.15 | $\gamma_s^d(\mathcal{S}) = -0.0026\mathcal{S} + 52.94$ | 2.6 | 52.94 | 0.9633 |
| 353.15 | $\gamma_s^d(\mathcal{S}) = -0.0022\mathcal{S} + 50.43$ | 2.2 | 50.43 | 0.9645 |
| 363.15 | $\gamma_s^d(\mathcal{S}) = -0.0018\mathcal{S} + 47.88$ | 1.8 | 47.88 | 0.9654 |
| 373.15 | $\gamma_s^d(\mathcal{S}) = -0.0014\mathcal{S} + 45.29$ | 1.4 | 45.29 | 0.9653 |
| 383.15 | $\gamma_s^d(\mathcal{S}) = -0.001\mathcal{S} + 42.65$ | 1.0 | 42.65 | 0.9602 |

Table 6 Temperature dependence of the surface-area derivative and of the extrapolated dispersive surface energy

| Equations | Units | $R^2$ |
|---|---|---|
| $\varepsilon_s^d(T) = \left(\frac{\partial\gamma_s^d}{\partial\mathcal{S}}\right) = -4\times10^{-5}T + 1.63\times10^{-2}$ | mJ g m$^{-4}$ | 1.0000 |
| $\gamma_s^d(\mathcal{S}_0,T) = -0.252T + 139.13$ | mJ m$^{-2}$ | 0.9998 |
| $\left(\frac{\partial\gamma_s^d(\mathcal{S},T)}{\partial T}\right)_{\mathcal{S}} = -4\times10^{-5}\mathcal{S} - 0.252$ | mJ m$^{-2}$ K$^{-1}$ | 0.9998 |
| $\left(\frac{\partial^2\gamma_s^d}{\partial T\partial\mathcal{S}}\right) = -4\times10^{-5}$ | mJ g m$^{-4}$ K$^{-1}$ | — |

Tables 5 and 6 demonstrate that the London dispersive surface energy of DVB-based copolymers is not only temperature-dependent, as classically expected for dispersive surface energetics, but also systematically morphology-dependent through the specific surface area $\mathcal{S}$. The combined dependence is accurately described by the bilinear energetic expression:

$$\gamma_s^d(T,\mathcal{S}) = \left(-4.0\times10^{-5}T + 1.63\times10^{-2}\right)\mathcal{S} - 0.252T + 139.13\left(\text{mJ m}^{-2}\right) \quad (26)$$

This equation is the energetic analogue of the bilinear adsorption–distance model $r_{S/X}(T,\mathcal{S})$: it is linear in $T$, linear in $\mathcal{S}$, and contains a coupling term $T\mathcal{S}$ that quantifies how morphology modulates the temperature sensitivity of dispersive surface energy.

(1) Meaning of $\varepsilon_s^d(T) = \left(\partial\gamma_s^d/\partial\mathcal{S}\right)_T$

The surface-area derivative

$$\varepsilon_s^d(T) = \left(\frac{\partial\gamma_s^d}{\partial\mathcal{S}}\right)_T = -4\times10^{-5}T + 1.63\times10^{-2} \quad (27)$$

is a central new observable: it measures the morphological sensitivity of dispersive surface energy at a fixed temperature. The perfect linearity ($R^2$ = 1.0000) indicates that the influence of accessible surface area on dispersive energetics is not random or probe-dependent noise, but a deterministic thermodynamic response of the DVB network.

The negative slope $-4\times10^{-5}$ implies that, as temperature increases, the ability of morphology (SSA) to enhance $\gamma_s^d$ diminishes. Physically, this is consistent with thermal agitation progressively reducing the effectiveness of short-range segment–segment cohesive interactions that underlie London dispersion at the polymer surface. In other words, at higher $T$, increasing $\mathcal{S}$ adds less "effective dispersive cohesion" per unit surface area than at lower $T$.

The positive intercept $1.63\times10^{-2}$ indicates that at low-to-moderate temperatures, higher $\mathcal{S}$ correlates with higher dispersive surface energy, consistent with a greater contribution of aromatic-rich surface patches and a larger fraction of "high-cohesion" adsorption environments exposed in more porous/hyper-cross-linked morphologies.

(2) Intrinsic dispersive surface energy at $\mathcal{S} = 0$: $\gamma_s^d(\mathcal{S}_0,T)$

The term

$$\gamma_s^d(\mathcal{S}_0,T) = -0.252T + 139.13\left(\text{mJ m}^{-2}\right) \quad (28)$$

represents the extrapolated dispersive surface energy in the limit of zero surface area contribution (formally $\mathcal{S}\to0$). While $\mathcal{S}=0$ is not physically realizable, this intercept is extremely meaningful: it isolates the pure temperature-driven component of the dispersive surface energy that is independent of morphology.

The magnitude of the slope ($-0.252$ mJ m$^{-2}$ K$^{-1}$) is large and highly linear ($R^2$ = 0.9998), evidencing that the dispersive component of the DVB surface behaves like a well-defined thermodynamic surface phase with a nearly constant dispersive surface entropy over the explored temperature window. In this view, 139.13 mJ m$^{-2}$ is the extrapolated intrinsic dispersive surface energy at 0 K (within the linear approximation), reflecting the cohesive strength of the aromatic DVB framework in the absence of thermal agitation.

(3) Temperature derivative at fixed surface area: dispersive surface entropy as a function of morphology

From the bilinear law, the temperature derivative at fixed $\mathcal{S}$ is:

$$\left(\frac{\partial\gamma_s^d(T,\mathcal{S})}{\partial T}\right)_{\mathcal{S}} = -4\times10^{-5}\mathcal{S} - 0.252\left(\text{mJ m}^{-2}\text{ K}^{-1}\right) \quad (29)$$

This result is particularly powerful because it shows that the effective dispersive surface entropy (magnitude of the temperature slope) is itself morphology dependent. Specifically, increasing $\mathcal{S}$makes the slope more negative, meaning that high-$\mathcal{S}$ copolymers lose dispersive surface energy slightly faster with temperature than low-$\mathcal{S}$ copolymers.

This has a clear physical interpretation: surfaces with larger accessible area tend to expose a broader distribution of adsorption environments, including thinner polymer segments, edges

of micropores, and more weakly constrained surface moieties. These environments are expected to be more thermally responsive, causing dispersive cohesion (and thus $\gamma_s^d$) to decay more strongly with temperature. The term $-4\times10^{-5}\mathcal{S}$ therefore quantifies the morphology-controlled contribution to dispersive surface entropy.

(4) Mixed second derivative: the energetic coupling constant

The mixed second derivative is constant:

$$\frac{\partial^2\gamma_s^d}{\partial T\partial\mathcal{S}} = -4\times10^{-5}\left(\text{mJ g m}^{-4}\text{ K}^{-1}\right) \quad (30)$$

This quantity is the direct energetic analogue of the adsorption–distance coupling coefficient $a_1 = \partial^2 r_{X/S}/(\partial\mathcal{S}\partial T)$. Here it provides the fundamental morphology–temperature coupling constant for dispersive surface energy.

• Its negative sign establishes that morphology and temperature act in an antagonistic way: increasing $\mathcal{S}$ increases $\gamma_s^d$, but this morphology-driven enhancement becomes weaker as temperature rises.

• Its constancy (no additional curvature in $T$ or $\mathcal{S}$) indicates that, over the explored domain, the DVB copolymer surfaces behave as a bilinear thermodynamic surface phase, *i.e.*, the coupling is first-order and uniform rather than changing regime with temperature or specific surface area.

(5) Conceptual significance: ''energetic bilinear coupling'' as a morphology–temperature fingerprint

The key conceptual advance is that these results establish $\gamma_s^d$ as a two-variable thermodynamic function:

$$\gamma_s^d = \gamma_s^d(T,\mathcal{S}) \quad (31)$$

rather than a purely temperature-dependent material constant. The presence of the $T\mathcal{S}$ coupling term is a clear fingerprint that dispersive surface energetics are governed by coupled effects of: thermal agitation (reducing cohesive interactions), and accessible morphology (controlling exposure of dispersive domains and the distribution of interaction environments).

In practical terms, this means that dispersive surface energy comparisons across copolymers are incomplete if reported at only one temperature or without specifying $\mathcal{S}$: two samples may display similar $\gamma_s^d$ at a given $T$ but possess different morphology-driven entropic slopes, which will cause their dispersive behavior to diverge at other temperatures.

Overall, Tables 5 and 6 reveal that the dispersive surface energy of DVB-based copolymers exhibits a bilinear dependence on temperature and specific surface area, with a constant mixed derivative $\partial^2\gamma_s^d/(\partial T\partial\mathcal{S})$. This constant defines an energetic morphology–temperature coupling, demonstrating that accessible surface area not only shifts the magnitude of $\gamma_s^d$ but also modulates its thermal decay. The bilinear energetic law therefore provides a compact thermodynamic framework for predicting dispersive surface energetics across copolymers of different morphologies within a unified and experimentally grounded description.

### 3.5. Unified thermomechanical–energetic framework of adsorption on DVB-based copolymers

The combined analysis of adsorption distance and dispersive surface energy establishes a unified thermomechanical–energetic description of solvent adsorption on DVB-based copolymers. The adsorption distance $r_{S/X}(T,\mathcal{S})$ was shown to obey a bilinear dependence on temperature and specific surface area, reflecting the coupled influence of thermal agitation and surface morphology on the equilibrium configuration of adsorbed molecules. Independently, the London dispersive surface energy $\gamma_s^d(T,\mathcal{S})$ exhibits the same bilinear structure, with linear decay in temperature at fixed surface area and linear decrease with surface area at fixed temperature, while the surface-area derivative $\varepsilon_s^d(T) = -\left(\partial\gamma_s^d/\partial\mathcal{S}\right)_T$ itself varies linearly with temperature. These parallel bilinear behaviors demonstrate that temperature and morphology do not act as separable variables but are intrinsically coupled through the same underlying thermomechanical mechanism. Increasing temperature weakens dispersion forces and increases adsorption distances through enhanced molecular fluctuations, whereas increasing surface area modifies both the intrinsic interaction strength and the mechanical compliance of adsorption sites, depending on the nature of the probe–surface interaction. The consistency between the bilinear forms of $r_{S/X}(T,\mathcal{S})$ and $\gamma_s^d(T,\mathcal{S})$ confirms that adsorption geometry, interaction energy, and entropy are governed by a common physical framework in which surface architecture controls how thermal energy is converted into mechanical dilation and energetic attenuation. This unified description provides a robust thermodynamic basis for predicting adsorption behavior on porous polymeric surfaces and rationalizes the observed differences between hyper-cross-linked and non-hyper-cross-linked networks in terms of morphology–temperature coupling.

### 3.6. Morphology-resolved enthalpy–entropy compensation in adsorption thermodynamics

To elucidate the fundamental link between copolymer morphology and adsorption thermodynamics, we examine the enthalpy–entropy compensation behavior as an explicit function of specific surface area (Tables S6 and S7). Rather than treating compensation as a fixed property of a given solid, the present analysis demonstrates that both the intrinsic compensation temperature and the enthalpic baseline are morphology-dependent quantities governed by quadratic specific surface area ($\mathcal{S}$) scaling.

(1) Robust enthalpy–entropy compensation across copolymers

To rationalize the adsorption thermodynamics across solvent families, the enthalpy–entropy compensation plots were examined for total, dispersive, and polar contributions (Fig. 1), and then relate the resulting compensation descriptors $T_{int}$ and $\Delta H_a^{\chi}(\Delta S_a^{\chi}=0)$ to copolymer specific surface area (Fig. 1).

For each polymer $P_i$, it was observed highly linear relationships of the form:

for the total standard adsorption variables:

$$\Delta H_a^0 = T_{int}\Delta S_a^0 + \Delta H_a^0(\Delta S_a^0 = 0) \quad (32)$$

and analogously for the dispersive and polar partitions:

$$\Delta H_a^d = T_{int}^d \Delta S_a^d + \Delta H_a^d(\Delta S_a^d = 0) \quad (33)$$

$$\Delta H_a^p = T_{int}^p \Delta S_a^p + \Delta H_a^p(\Delta S_a^p = 0) \quad (34)$$

This is more than a statistical correlation: it is direct thermodynamic evidence that, across a solvent family, adsorption proceeds along a compensation manifold where stronger enthalpic stabilization is accompanied by a proportional entropic

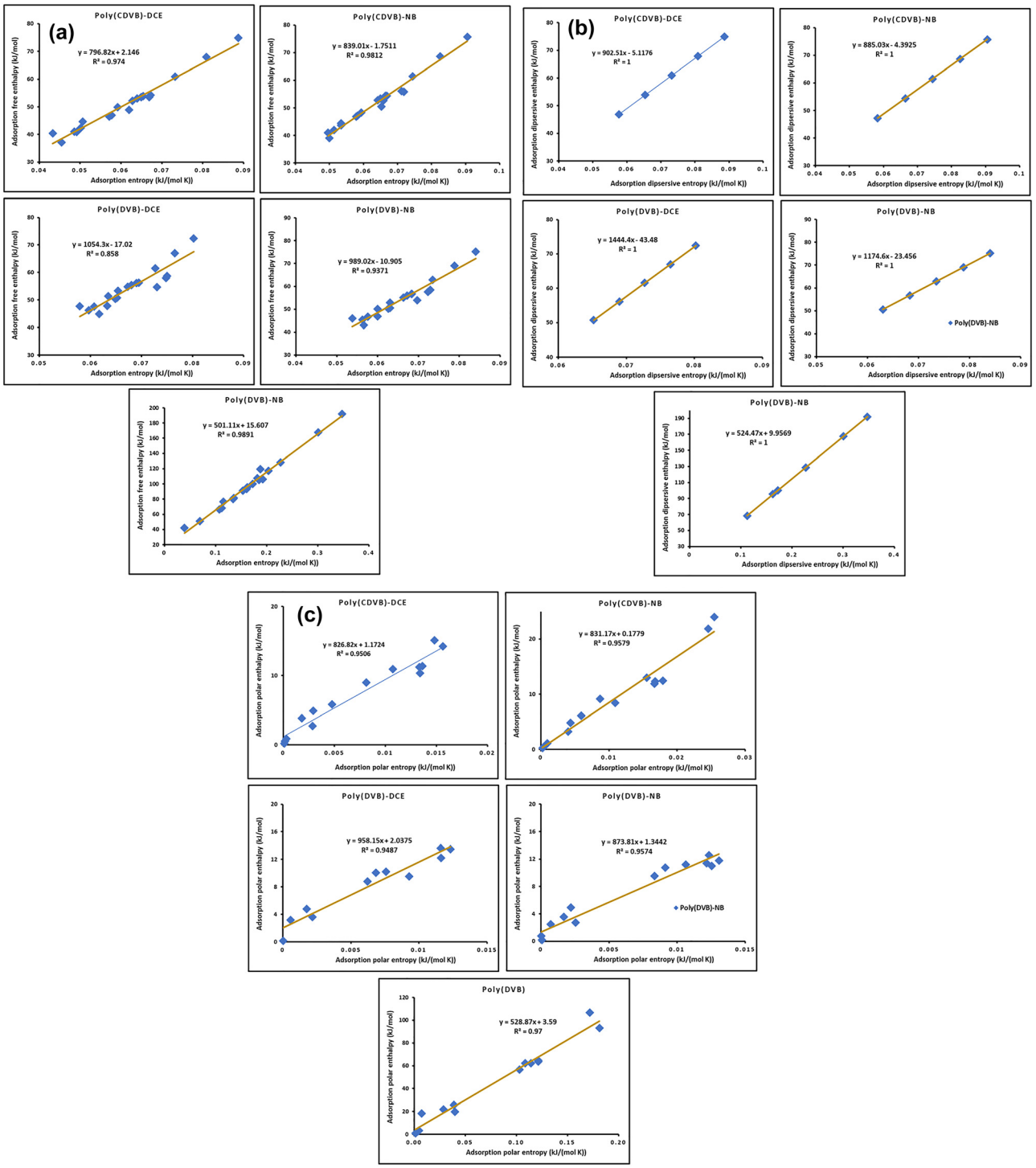


Fig. 1 Unified enthalpy–entropy compensation across adsorption channels and morphology control by specific surface area. (a) Enthalpy–entropy compensation for total adsorption ($\Delta H_a^0$ *vs.* $\Delta S_a^0$) obtained from all probe molecules on the five DVB-based copolymers. (b) Dispersive compensation ($\Delta H_a^d$ *vs.* $\Delta S_a^d$) obtained from *n*-alkanes, showing near-ideal linearity consistent with a single dispersion–ordering mechanism. (c) Polar compensation ($\Delta H_a^p$ *vs.* $\Delta S_a^p$) obtained from polar probes, reflecting the combined influence of specific interactions and induced polarization. In each panel, the slope defines the intrinsic (compensation) temperature $T_{int}$, while the intercept gives the enthalpic baseline $\Delta H_a^{\chi}(\Delta S_a^{\chi} = 0)$.

penalty (or *vice versa*). This was demonstrated simultaneously for:

- total adsorption (all probes),
- dispersive adsorption (*n*-alkanes),
- polar adsorption (polar probes),

meaning that compensation is not an artifact of mixing different solvent classes; it is an intrinsic signature of the polymer–probe interface.

The experimental results are presented in Table 7.

(2) Physical meaning of $T_{int}$: a thermodynamic ''coupling temperature''

The slope $T_{int}$ has a precise meaning:

- It quantifies the temperature at which enthalpic and entropic variations compensate across a series.
- It is a fingerprint of the dominant adsorption mechanism (confinement/packing *vs.* conformational freedom *vs.* specific interactions).

A high $T_{int}$ indicates that changes in enthalpy are strongly mirrored by changes in entropy, typical of adsorption processes controlled by structural organization (restricted configurations, packing in pores, segmental rearrangement). A lower $T_{int}$ indicates weaker coupling and more ''energetic-only'' variation. This shows a striking separation between polymers with different adsorption intrinsic temperatures $T_{int}$ (Table 7). Hyper-cross-linked CDVB systems exhibit a strongly coupled regime ($\sim$800–840 K), while DVB systems modified by post-cross-linking environments reach very large compensation temperatures ($\sim$990–1050 K), consistent with adsorption occurring in a more heterogeneous and confinement-sensitive landscape. In contrast, the reference poly(DVB) exhibits a much lower $T_{int}$ ($\sim$ 500 K), consistent with a more compliant/accessible surface where adsorption variations are less dominated by entropic restriction.

(3) Meaning of $\Delta H_a^{\chi}(\Delta S_a^{\chi} = 0)$: intrinsic ''enthalpic baseline'' at zero entropic cost

The intercept $\Delta H_a^{\chi}(\Delta S_a^{\chi} = 0)$ is extremely valuable. It corresponds to an enthalpic baseline: what remains of adsorption enthalpy when the entropic term vanishes in the compensation projection. It is therefore sensitive to the intrinsic cohesive interactions of the surface (aromatic dispersion, polarizability, and local binding strength) rather than confinement-driven entropy.

- Positive values suggest a baseline enthalpic stabilization even without entropic change.

Table 7 Linear regressions of the adsorption enthalpy as a function of the corresponding adsorption entropy, $\Delta H_a^{\chi} = T_{int}^{\chi}\Delta S_a^{\chi} + \Delta H_a^{\chi}(\Delta S_a^{\chi} = 0)$, are reported for the total ($\chi$ = 0), dispersive ($\chi$ = *d*, *n*-alkanes), and polar ($\chi$ = *p*, polar probes) contributions. The slope $T_{int}^{\chi}$ represents the intrinsic (compensation) temperature characterizing the enthalpy–entropy coupling of adsorption, while the intercept $\Delta H_a^{\chi}(\Delta S_a^{\chi} = 0)$ corresponds to the extrapolated enthalpic baseline at zero entropic contribution. The coefficient of determination ($R^2$) quantifies the validity of the compensation behavior for each copolymer and interaction channel

Variations of total adsorption enthalpy $\Delta H_a^0 = f(\Delta S_a^0)$ and adsorption parameters

| Copolymer | Equation | $T_{int}^0$ | $\Delta H_a^0(\mathcal{S}, \Delta S_a^0 = 0)$ | $R^2$ |
|---|---|---|---|---|
| Poly(DVB) | $\Delta H_a^0 = 501.11\Delta S_a^0 + 15.61$ | 501.11 | 15.61 | 0.9891 |
| Poly(DVB)–NB | $\Delta H_a^0 = 989.02\Delta S_a^0 - 10.901$ | 989.02 | −10.91 | 0.9371 |
| Poly(CDVB)–NB | $\Delta H_a^0 = 839.01\Delta S_a^0 - 1.75$ | 839.01 | −1.75 | 0.9812 |
| Poly(CDVB)–DCE | $\Delta H_a^0 = 796.82\Delta S_a^0 + 2.15$ | 796.82 | 2.15 | 0.974 |
| Poly(DVB)–DCE | $\Delta H_a^0 = 1054.3\Delta S_a^0 - 17.02$ | 1054.3 | 17.02 | 0.858 |
| Equations in $\mathcal{S}$ | $T_{int}^0(\mathcal{S}) = -1.10^{-4}\mathcal{S}^2 + 1.097\mathcal{S} - 257.44$ | | $\Delta H_a^0(\mathcal{S}, \Delta S_a^0 = 0) = 4.10^{-4}\mathcal{S}^2 - 0.84\mathcal{S} + 430.79$ | |
| $R^2$ | $R^2$ = 0.7766 | | $R^2$ = 0.975 | |

Variations of dispersive adsorption enthalpy $\Delta H_a^d = f(\Delta S_a^d)$ and dispersive parameters

| Copolymer | Equation | $T_{int}^d$ | $\Delta H_a^d(\Delta S_a^d = 0)$ | $R^2$ |
|---|---|---|---|---|
| Poly(DVB) | $\Delta H_a^d = 524.47\Delta S_a^d + 9.96$ | 524.47 | 9.96 | 1.0000 |
| Poly(DVB)–NB | $\Delta H_a^d = 1174.6\Delta S_a^d - 23.46$ | 1174.6 | −23.46 | 1.0000 |
| Poly(CDVB)–NB | $\Delta H_a^d = 885.03\Delta S_a^d - 4.39$ | 885.03 | −4.39 | 1.0000 |
| Poly(CDVB)–DCE | $\Delta H_a^d = 902.51\Delta S_a^d - 5.12$ | 902.51 | −5.12 | 1.0000 |
| Poly(DVB)–DCE | $\Delta H_a^d = 1444.4\Delta S_a^d - 43.48$ | 1444.4 | −43.48 | 1.0000 |
| Equations in $\mathcal{S}$ | $T_{int}^d(\mathcal{S}) = 2.6.10^{-3}\mathcal{S}^2 - 4.3246\mathcal{S} + 2321.1$ | | $\Delta H_a^d(\mathcal{S}, \Delta S_a^d = 0) = -2.10^{-4}\mathcal{S}^2 + 0.43\mathcal{S} - 182.73$ | |
| $R^2$ | $R^2$ = 0.797 | | $R^2$ = 0.7033 | |

Variations of polar adsorption enthalpy $\Delta H_a^p = f(\Delta S_a^p)$ and polar parameters

| Copolymer | Equation | $T_{int}^p$ | $\Delta H_a^p(\Delta S_a^p = 0)$ | $R^2$ |
|---|---|---|---|---|
| Poly(DVB) | $\Delta H_a^p = 528.87\Delta S_a^p + 3.59$ | 528.87 | 3.590 | 0.97 |
| Poly(DVB)–NB | $\Delta H_a^p = 873.81\Delta S_a^p + 1.3442$ | 873.81 | 1.344 | 0.9574 |
| Poly(CDVB)–NB | $\Delta H_a^p = 831.17\Delta S_a^p + 0.1779$ | 831.17 | 0.178 | 0.9579 |
| Poly(CDVB)–DCE | $\Delta H_a^p = 826.82\Delta S_a^p + 1.1724$ | 826.82 | 1.172 | 0.9506 |
| Poly(DVB)–DCE | $\Delta H_a^p = 958.15\Delta S_a^p + 2.0375$ | 958.15 | 2.038 | 0.9487 |
| Equations in $\mathcal{S}$ | $T_{int}^p(\mathcal{S}) = 4.10^{-5}\mathcal{S}^2 + 0.560\mathcal{S} + 69.40$ | | $\Delta H_a^p(\mathcal{S}, \Delta S_a^p = 0) = 2.10^{-5}\mathcal{S}^2 - 0.054\mathcal{S} + 31.16$ | |
| $R^2$ | $R^2$ = 0.9366 | | $R^2$ = 0.8534 | |

• Negative values indicate that the compensation line extrapolates into a regime where entropic effects dominate the effective stabilization.

The total adsorption intercepts span from about −17 to +16 kJ mol$^{-1}$ (depending on polymer), which is physically consistent with polymer surfaces where the observed adsorption thermodynamics are strongly reweighted by entropic restriction and site heterogeneity.

(4) Dispersive compensation is "perfect": $R^2$ = 1 for *n*-alkanes is a major mechanistic result

For the dispersive channel, $R^2$ values are 1.0000 for all copolymers. This means that *n*-alkane adsorption on each polymer is governed by a single dominant physical mechanism over the whole homologous series, *i.e.*, London dispersion interactions + packing/ordering (entropy), with minimal interference from chemical specificity. The dispersive $T_{int}^{d}$ values vary widely (Table 6). As the architecture evolves from the relatively "open" poly(DVB) to the more constrained/responsive post-cross-linked networks, dispersive adsorption becomes increasingly controlled by entropy of confinement/ordering in addition to pure dispersion energy. The very high $T_{int}^{d}$ values (1175–1444 K) strongly imply that the dominant variability among *n*-alkanes is not merely their polarizability (enthalpy), but the increasing entropic restriction of larger chains within the adsorption environment.

This strongly supports this thermomechanical picture: dispersion-dominated adsorption is not purely energetic; it has a strong entropic structural component.

(5) Polar compensation is strong but shows polymer-dependent heterogeneity

The results confirm that polar adsorption obeys a clear compensation law on each copolymer:

$$\Delta H_a^p = T_{int}^p \Delta S_a^p + \Delta H_a^p(\Delta S_a^p = 0) \quad (35)$$

with high regression quality for all materials ($R^2 \approx 0.95$–$0.97$). This indicates that, despite the multiplicity of polar interaction channels (dipole–dipole, dipole–induced dipole, donor–acceptor, and polarization/relaxation effects), the ensemble of polar probes samples the copolymer surfaces along a single dominant thermodynamic manifold in the ($\Delta H^p$,$\Delta S^p$) space for each copolymer.

Importantly, the dispersion in slopes and intercepts across copolymers is systematic rather than random, implying that polymer chemistry/morphology tunes the strength of enthalpy–entropy coupling rather than breaking the compensation regime. The corresponding $T_{int}^{p}$ values are given in Table 6. This intrinsic temperature $T_{int}^{p}$ reflects how strongly enthalpic stabilization is accompanied by entropic restriction for polar adsorption. This ordering (from $T_{int}^{p}$ = 528.9 K to $T_{int}^{p}$ = 958.2 K) strongly supports a mechanistic picture in which increasing cross-linking/post-cross-linking architecture increases the extent of interfacial organization (restricted orientations, reduced configurational freedom, stronger induced polarization), thereby raising $T_{int}^{p}$. In contrast, the lower value for poly(DVB) indicates a more compliant adsorption environment in which polar probes experience weaker coupling between energy gain and entropic penalty.

Thus, $T_{int}^{p}$ can be interpreted as a thermodynamic signature of polarization/structuring sensitivity, *i.e.*, how strongly the surface reorganizes (and constrains polar probe configurations) when adsorption strength increases.

(6) Quadratic dependence on specific surface area $\mathcal{S}$

It was observed that both $T_{int}$ and $\Delta H(\Delta S = 0)$ exhibit quadratic trends *versus* specific surface area *S*. This is highly meaningful:

• A linear dependence would suggest a simple "more surface area → proportional change."

• Quadratic behavior implies two competing morphological contributions that scale differently with SSA, such as:

(1) Accessible aromatic cohesive domains (increasing $\gamma_s^d$, strengthening enthalpy)

(2) Confinement/heterogeneity and restricted configurations (increasing entropic penalty, raising $T_{int}$)

(3) Micro/mesopore balance and site-type mixing (curvature arising from changing fractions of site families with $\mathcal{S}$)

Thus, $\mathcal{S}$ is not merely a geometric descriptor here: it is a proxy for the distribution of adsorption environments. The curvature indicates that when $\mathcal{S}$ increases, the type of surface encountered by probes (*e.g.*, more microporous domains, more edges, more constrained segments) changes, which naturally generates nonlinearity. Notably:

• The total adsorption: $\Delta H(\Delta S = 0)$ *versus* $\mathcal{S}$ shows a very high $R^2$ ($\sim$0.975), meaning the "enthalpic baseline" is tightly controlled by morphology.

• The dispersive and polar channels show moderate-to-strong $R^2$ for these quadratic laws, consistent with additional sensitivity to chemical heterogeneity and specific interaction modes.

(7) Key conceptual synthesis

The obtained results support a unified mechanistic picture:

• Dispersive adsorption is governed by an almost "ideal" compensation line ($R^2$ = 1), revealing a single dominant dispersion–ordering mechanism, with $\mathcal{S}$ controlling how strongly ordering/confinement contributes.

• Polar adsorption exhibits strong compensation but with polymer-dependent scatter, revealing multiple interaction channels consistent with heterogeneity and induced polarization.

• Total adsorption sits between both, as expected from the superposition of dispersive and polar contributions.

The emergence of $T_{int}$ as a function of $\mathcal{S}$, and particularly its quadratic dependence, establishes a direct bridge between polymer morphology and adsorption thermodynamics. This shows that $\mathcal{S}$ is not only a geometric parameter—it is a thermodynamic control knob governing the enthalpy–entropy partitioning of adsorption.

(8) Mathematical structure: a bilinear law with quadratic morphology control

It was proved that each adsorption channel $\chi \in \{0, d, p\}$ follows an enthalpy–entropy compensation law:

$$\Delta H_a^{\chi}(\mathcal{S}) = T_{int}^{\chi}(\mathcal{S})\Delta S_a^{\chi} + \Delta H_a^{\chi}\left(\mathcal{S}, \Delta S_a^{\chi} = 0\right) \quad (36)$$

with $\mathcal{S}$-controlled descriptors:

$$T_{\mathrm{int}}^{\chi}(\mathcal{S}) = a_1^{\chi}\mathcal{S}^2 + b_1^{\chi}\mathcal{S} + c_1^{\chi} \quad (37)$$

$$\Delta H_{\mathrm{a}}^{\chi}\left(\mathcal{S}, \Delta S_{\mathrm{a}}^{\chi} = 0\right) = a_2^{\chi}\mathcal{S}^2 + b_2^{\chi}\mathcal{S} + c_2^{\chi} \quad (38)$$

Therefore,

$$\Delta H_{\mathrm{a}}^{\chi}(\mathcal{S}) = \left(a_1^{\chi}\mathcal{S}^2 + b_1^{\chi}\mathcal{S} + c_1^{\chi}\right)\Delta S_{\mathrm{a}}^{\chi} + \left(a_2^{\chi}\mathcal{S}^2 + b_2^{\chi}\mathcal{S} + c_2^{\chi}\right) \quad (39)$$

The obtained experimental values of constants $a_1^{\chi}$, $b_1^{\chi}$, $c_1^{\chi}$, $a_2^{\chi}$, $b_2^{\chi}$, and $c_2^{\chi}$ are given in Table 7.

Eqn (39) is a bilinear model in the variables $\left(\Delta S_{\mathrm{a}}^{\chi}, \mathcal{S}\right)$ but with quadratic dependence on $\mathcal{S}$. At fixed $\mathcal{S}$: $\Delta H_{\mathrm{a}}^{\chi}$ is strictly linear in $\Delta S_{\mathrm{a}}^{\chi}$ (pure compensation line) across different morphologies: both the slope and the intercept of the compensation line evolve nonlinearly with $\mathcal{S}$.

All coefficients were obtained from regression analysis of inverse gas chromatography data over the investigated temperature range and across all copolymer types and probe molecules. The reported uncertainties in Table 8 represent 95% confidence intervals, demonstrating the high statistical significance and robustness of the fitted parameters.

The sign and magnitude of the coefficients reflect the strength of thermomechanical coupling between temperature and specific surface area, while the non-zero quadratic terms confirm the presence of second-order morphology effects governing adsorption thermodynamics. The clear differentiation between dispersive, polar, and total channels further supports the physical consistency of the proposed framework.

**3.6.1. Statistical reliability of thermomechanical and compensation parameters.** The statistical robustness of the thermomechanical and compensation coefficients was assessed through regression analysis across all copolymers and probe molecules. The parameters $a_i^{\chi}$, $b_i^{\chi}$, and $c_i^{\chi}$ were determined with 95% confidence intervals, as reported in Table 8. The relatively small uncertainties associated with these coefficients—typically below a few percent—demonstrate the high precision of the experimental data and the reliability of the fitted models.

In particular, the thermomechanical coupling coefficient $a_1^{\chi}$, which governs the interaction between temperature and surface morphology, is determined with high accuracy for all interaction channels. The clear separation between dispersive, polar, and total values of $a_1^{\chi}$ confirms that the model captures distinct physical regimes of adsorption.

These results provide strong statistical evidence that the bilinear thermomechanical formulation and the quadratic compensation framework constitute robust and reproducible descriptions of adsorption thermodynamics on DVB-based copolymers.

The narrow confidence intervals obtained for all coefficients confirm that the observed thermomechanical and compensation behaviors are intrinsic properties of the system rather than fitting artifacts.

To rigorously assess the functional dependence of the compensation parameters on the specific surface area, alternative fitting models—including linear, exponential, and quadratic formulations—were systematically evaluated. The results of this comparative analysis are summarized in Table 9, which reports the corresponding equations and statistical indicators for each interaction channel.

The coefficient of determination ($R^2$) is reported for each model. The quadratic formulation consistently provides the highest predictive accuracy, particularly for the enthalpy term, where linear and exponential models fail to reproduce the experimental trends.

These results demonstrate that the quadratic dependence reflects intrinsic second-order morphology effects governing adsorption thermodynamics, rather than a simple empirical fit.

To validate the functional dependence of the compensation parameters on the specific surface area, linear, exponential, and quadratic models were systematically compared (Table 9). The results clearly demonstrate that the quadratic formulation provides the most accurate and consistent description across all interaction channels.

The superiority of the quadratic model is particularly pronounced for the reference enthalpy, where the coefficient of determination increases dramatically (*e.g.*, $R^2$ = 0.975 for total adsorption), while linear and exponential models fail to capture the observed behavior. This confirms that the morphology dependence of adsorption thermodynamics involves intrinsic curvature, reflecting second-order effects associated with pore structure evolution and interaction heterogeneity.

(9) Derivative meaning: experimental ''sensitivities'' and coupling constants

The derivative identities have clear mechanistic meanings:

– Entropy sensitivity at fixed morphology with:

$$\left(\frac{\partial \Delta H_{\mathrm{a}}^{\chi}}{\partial \Delta S_{\mathrm{a}}^{\chi}}\right)_{\mathcal{S}} = T_{\mathrm{int}}^{\chi}(\mathcal{S}) \quad (40)$$

This compensation temperature is the experimental enthalpy-per-entropy sensitivity at a given $\mathcal{S}$. The second derivative

Table 8 Thermomechanical and compensation coefficients (±95% confidence intervals) for total, dispersive, and polar adsorption. Parameters describe the morphology dependence of intrinsic temperature and reference enthalpy, confirming robust second-order thermodynamic coupling

| Channel $\chi$ | Total adsorption parameters (0) | Dispersive parameters ($d$) | Polar parameters ($p$) |
|---|---|---|---|
| $a_1^{\chi}$ | $-1.0 \times 10^{-4} \pm 2 \times 10^{-6}$ | $2.6 \times 10^{-3} \pm 5 \times 10^{-5}$ | $4.0 \times 10^{-5} \pm 8 \times 10^{-7}$ |
| $b_1^{\chi}$ | $1.097 \pm 0.022$ | $-4.33 \pm 0.09$ | $0.560 \pm 0.011$ |
| $c_1^{\chi}$ | $-257.44 \pm 5.15$ | $2321.1 \pm 46.4$ | $69.40 \pm 1.39$ |
| $a_2^{\chi}$ | $-4.0 \times 10^{-4} \pm 8 \times 10^{-6}$ | $-2.0 \times 10^{-3} \pm 4 \times 10^{-6}$ | $2.0 \times 10^{-5} \pm 4 \times 10^{-7}$ |
| $b_2^{\chi}$ | $-0.838 \pm 0.017$ | $0.430 \pm 0.009$ | $-0.054 \pm 0.001$ |
| $c_2^{\chi}$ | $430.79 \pm 8.62$ | $-182.73 \pm 3.66$ | $31.16 \pm 0.62$ |

Table 9 Comparative evaluation of functional models for morphology-dependent thermodynamic parameters. Comparison of linear, exponential, and quadratic models describing the dependence of intrinsic temperature $T_{int}^{\chi}(\mathcal{S})$ and reference enthalpy $\Delta H_a^{\chi}(\mathcal{S}, \Delta S = 0)$ on the specific surface area for total ($\chi$ = 0), dispersive ($\chi$ = *d*), and polar ($\chi$ = *p*) interaction channels

| Equations of total parameters $T_{int}$ and DH as a function of specific surface area | | | | |
|---|---|---|---|---|
| Interpolation | $T_{int}^{0}(\mathcal{S})$ | $R^2$ | $\Delta H_a^0(\mathcal{S}, \Delta S_a^{\chi} = 0)$ | $R^2$ |
| Exponential | $T_{int}^{0}(\mathcal{S}) = 213.74\exp(0.0011\mathcal{S})$ | 0.6308 | $\Delta H_a^0 = -18.82\ln(\mathcal{S}) + 137.39$ | 0.1386 |
| Linear | $T_{int}^{0}(\mathcal{S}) = 0.7857\mathcal{S} - 103.29$ | 0.6362 | $\Delta H_a^0 = -0.0161\mathcal{S} + 23.649$ | 0.1069 |
| Quadratic | $T_{int}^{0}(\mathcal{S}) = -0.0001\mathcal{S}^2 + 1.097\mathcal{S} - 257.44$ | 0.6766 | $\Delta H_a^0 = 0.0004\mathcal{S}^2 - 0.8376x + 430.79$ | 0.975 |
| Equations of dispersive parameters $T_{int}$ and DH as a function of specific surface area | | | | |
| Interpolation | $T_{int}^{d}(\mathcal{S})$ | $R^2$ | $\Delta H_a^d(\mathcal{S}, \Delta S_a^{\chi} = 0)$ | $R^2$ |
| Exponential | $T_{int}^{d}(\mathcal{S}) = 176.39\exp(0.0014\mathcal{S})$ | 0.679 | $\Delta H_a^d = -60.9\ln(\mathcal{S}) + 417.08$ | 0.4799 |
| Linear | $T_{int}^{d}(\mathcal{S}) = 1.1551\mathcal{S} - 394.75$ | 0.6513 | $\Delta H_a^d = -0.0606\mathcal{S} + 59.193$ | 0.5021 |
| Quadratic | $T_{int}^{d}(\mathcal{S}) = 0.0026\mathcal{S}^2 - 4.3246\mathcal{S} + 2321.1$ | 0.797 | $\Delta H_a^d = -0.0002\mathcal{S}^2 + 0.428\mathcal{S} - 182.73$ | 0.7033 |
| Equations of polar parameters $T_{int}$ and DH as a function of specific surface area | | | | |
| Interpolation | $T_{int}^{p}(\mathcal{S})$ | $R^2$ | $\Delta H_a^p(\mathcal{S}, \Delta S_a^{\chi} = 0)$ | $R^2$ |
| Exponential | $T_{int}^{p}(\mathcal{S}) = 257.38\exp(0.0009\mathcal{S})$ | 0.9105 | $\Delta H_a^p = 15.186e^{-0.002x}$ | 0.6507 |
| Linear | $T_{int}^{p}(\mathcal{S}) = 0.6525\mathcal{S} + 23.73$ | 0.9026 | $\Delta H_a^p = -0.004\mathcal{S} + 6.4103$ | 0.5719 |
| Quadratic | $T_{int}^{p}(\mathcal{S}) = 4 \times 10^{-5}\mathcal{S}^2 + 0.5603\mathcal{S} + 69.403$ | 0.9366 | $\Delta H_a^p = 2 \times 10^{-5}\mathcal{S}^2 - 0.0539\mathcal{S} + 31.155$ | 0.8534 |

$\left(\frac{\partial^2 \Delta H_a^{\chi}}{\partial(\Delta S_a^{\chi})^2}\right)_{\mathcal{S}} = 0$ means that no curvature in $\Delta H_a^{\chi}$ *versus* $\Delta S_a^{\chi}$ at fixed SSA: one dominant compensation regime per channel.

– Morphology sensitivity at fixed entropy

$$\left(\frac{\partial(\Delta H_a^{\chi})}{\partial \mathcal{S}}\right)_{\Delta S_a^{\chi}} = \left(2a_1^{\chi}\mathcal{S} + b_1^{\chi}\right)\Delta S_a^{\chi} + \left(2a_2^{\chi}\mathcal{S} + b_2^{\chi}\right) \quad (41)$$

where $\mathcal{S}$ affects enthalpy through two mechanisms:

(1) *via* the slope $T_{int}^{\chi}(\mathcal{S})$ (the term $\left(2a_1^{\chi}\mathcal{S} + b_1^{\chi}\right)\Delta S_a^{\chi}$), meaning morphology changes the strength of enthalpy–entropy coupling;

(2) *via* the intercept $\Delta H_a^{\chi}(\mathcal{S}, \Delta S_a^{\chi} = 0)$ (the term $2a_2^{\chi}\mathcal{S} + b_2^{\chi}$), meaning morphology changes the cohesive enthalpic baseline even at zero entropic projection.

– Mixed derivative: the morphology–compensation coupling

$$\left(\frac{\partial^2(\Delta H_a^{\chi})}{\partial(\Delta S_a^{\chi})\partial \mathcal{S}}\right)_{\mathcal{S},\Delta S_a^{\chi}} = \left(2a_1^{\chi}\mathcal{S} + b_1^{\chi}\right) \quad (42)$$

This quantifies how strongly morphology changes the compensation slope. It is the enthalpy–entropy counterpart of the earlier coupling constants $a_1 = \partial^2 r_{X/S}/(\partial \mathcal{S}\partial T)$ and $\partial^2\gamma/(\partial T\partial \mathcal{S})$.

– Curvature in morphology (SSA)

$$\left(\frac{\partial^2(\Delta H_a^{\chi})}{\partial \mathcal{S}^2}\right)_{\Delta S_a^{\chi}} = 2a_1^{\chi}\Delta S_a^{\chi} + 2a_2^{\chi} \quad (43)$$

This result is powerful: the curvature of $\Delta H_a^{\chi}$ *vs.* $\mathcal{S}$ is not only from baseline structure ($a_2^{\chi}$)—it also depends on the entropy level through $a_1^{\chi}\Delta S_a^{\chi}$. That is exactly what "quadratic morphology control" means. And the third derivative

$$\left(\frac{\partial^3(\Delta H_a^{\chi})}{\partial(\Delta S_a^{\chi})\partial \mathcal{S}^2}\right)_{\mathcal{S},\Delta S_a^{\chi}} = 2a_1^{\chi} \quad (44)$$

shows that $a_1^{\chi}$ is the highest-order invariant controlling how morphology curvature propagates into the compensation slope.

To further elucidate the physical significance of the quadratic compensation framework, the thermodynamic coupling and curvature parameters were derived analytically from the fitted coefficients. These quantities, reported in Table 10, provide a quantitative description of the interplay between surface morphology and adsorption thermodynamics across the different interaction channels.

The results presented in Table 10 provide a quantitative interpretation of the thermodynamic structure of adsorption on DVB-based copolymers. The mixed derivative $\partial^2\Delta H_a^{\chi}/(\partial \mathcal{S}\partial\Delta S_a^{\chi})$ reveals the strength of coupling between surface morphology and entropy, and its magnitude varies significantly across interaction channels. For dispersive interactions, the relatively large coefficient ($5.2 \times 10^{-3}$) indicates strong sensitivity to surface area, consistent with confinement-driven ordering of non-polar molecules within microporous environments. In contrast, the polar contribution exhibits a much smaller coupling coefficient ($8.0 \times 10^{-5}$), reflecting weaker dependence on morphology and a greater influence of localized, specific interactions.

The curvature term $\partial^2\Delta H_a^{\chi}/\partial \mathcal{S}^2$ further highlights the presence of second-order morphology effects. The non-zero values confirm that adsorption thermodynamics cannot be described by linear scaling with surface area. Instead, the curvature reflects the progressive modification of adsorption environments as the accessible surface increases, including changes in pore connectivity, site distribution, and interaction cooperativity.

Table 10 Thermodynamic coupling and curvature parameters of adsorption compensation surfaces. Thermodynamic coupling and curvature parameters derived from the quadratic compensation framework for dispersive ($\chi = d$), polar ($\chi = p$), and total ($\chi = 0$) adsorption. The mixed derivative $\partial^2\Delta H_a^\chi/(\partial S\partial\Delta S_a^\chi)$ quantifies the strength of morphology–thermodynamics coupling, while the second derivative $\partial^2\Delta H_a^\chi/\partial S^2$ reflects the curvature of the compensation surface with respect to specific surface area. These parameters provide direct insight into confinement effects, interaction heterogeneity, and the balance between dispersive and polar contributions

| Interaction | Dispersive ($d$) | Polar ($p$) | Total (0) |
|---|---|---|---|
| Coupling $\frac{\partial^2\Delta H}{\partial S\partial\Delta S}$ | $5.2 \times 10^{-3}S - 4.33$ | $8.0 \times 10^{-5}S + 0.560$ | $-2.0 \times 10^{-4}S + 1.097$ |
| Curvature $\frac{\partial^2\Delta H}{\partial S^2}$ | $5.2 \times 10^{-3}\Delta S - 4.0 \times 10^{-3}$ | $8.0 \times 10^{-5}\Delta S + 4.0 \times 10^{-5}$ | $-2.0 \times 10^{-4}\Delta S - 8.0 \times 10^{-4}$ |
| Physical interpretation | Strong morphology-driven ordering and confinement effects | Moderate morphology sensitivity with interaction heterogeneity | Balanced regime combining dispersive and polar effects |

The total adsorption behavior emerges as a balanced regime, where the opposing trends of dispersive and polar contributions combine to produce intermediate coupling and curvature. This demonstrates that adsorption thermodynamics in DVB-based copolymers is governed by a subtle interplay between molecular interactions and structural organization, rather than by a single dominant mechanism.

Overall, these results establish that the compensation surface is not merely a mathematical construct, but a physically meaningful representation of morphology-controlled adsorption, where coupling and curvature parameters act as fundamental descriptors of the system.

The emergence of distinct coupling and curvature regimes confirms that adsorption thermodynamics is intrinsically governed by second-order morphology effects encoded in the polymer structure.

(10) Physical interpretation of the fitted coefficients

(a) Total adsorption ($\chi = 0$)

• $a_1^0 = -1.0 \times 10^{-4}$ (negative) $\Rightarrow$ the curvature of $T_{int}^0(\mathcal{S})$ is downward: as $\mathcal{S}$ increases, the strengthening of coupling saturates and eventually weakens. This is consistent with two competing effects: increased accessibility (more sites) *versus* increased thermal disorder/heterogeneity at very high $\mathcal{S}$.

• $b_1^0 = 1.097 > 0 \Rightarrow$ at moderate $\mathcal{S}$, $T_{int}^0$ increases with $\mathcal{S}$: adsorption becomes increasingly governed by coupled enthalpy–entropy effects (packing/confinement + polymer segment rearrangement).

• Intercept curvature: $a_2^0 = -0.0004$ (negative) $\Rightarrow \Delta H_a^0(\Delta S_a^0 = 0)$ is concave downward with $\mathcal{S}$: the ''enthalpic baseline'' initially increases/decreases linearly but exhibits saturation/turnover with increasing $\mathcal{S}$—again consistent with a site-mixture evolution rather than simple proportional scaling.

This physically means that the total adsorption on DVB copolymers is controlled by morphology through both (i) changes in the thermodynamic coupling regime (*via* $T_{int}(\mathcal{S})$) and (ii) changes in cohesive baseline (*via* $\Delta H_a^\chi(\mathcal{S}, \Delta S_a^\chi = 0)$). The negative $a_1^0$ and $a_2^0$ indicate diminishing returns of $\mathcal{S}$ at high surface areas.

(b) Dispersive adsorption ($\chi = d$, *n*-alkanes)

Here the standout result is:

• $a_1^d = +2.6 \times 10^{-3} > 0 \Rightarrow T_{int}^d(\mathcal{S})$ is strongly convex upward with $\mathcal{S}$.

• $b_1^d = -4.33$ and $c_1^d = 2321.1 \Rightarrow$ the function is large and sensitive: dispersive compensation temperature is extremely morphology-dependent.

This means that for *n*-alkanes, adsorption is dispersion-dominated but the variation across the homologous series is strongly governed by entropy of ordering/confinement within the polymer network. Increasing $\mathcal{S}$ in hyper-cross-linked structures typically corresponds to increased microporous content and stronger geometric constraints for chain packing. That naturally increases enthalpy–entropy coupling, explaining the positive $a_1^d$.

• Baseline term: $a_2^d = -2 \times 10^{-3} < 0$, $b_2^d = +0.43 \Rightarrow$ the cohesive dispersive baseline *vs.* $\mathcal{S}$ has a competing trend: initially increasing with $\mathcal{S}$ but curving downward at high $\mathcal{S}$. This matches the idea that very high $\mathcal{S}$ exposes more ''weakly cohesive'' edge/defect-like polymer segments that reduce the per-area cohesive baseline, even while confinement effects increase coupling.

Therefore, the dispersive adsorption shows the clearest separation between ''cohesive baseline'' and ''confinement-coupling'', and $\mathcal{S}$ primarily tunes the entropic organization contribution of *n*-alkane adsorption.

(c) Polar adsorption ($\chi = p$)

The intercepts $\Delta H_a^p(\Delta S_a^p = 0)$ are small and positive: 0.18–3.59 kJ mol$^{-1}$. These represent an extrapolated enthalpic baseline of polar adsorption at vanishing entropic term within the compensation projection. Their modest magnitude is physically plausible for the ''pure polar reference'' contribution: polar stabilization is present but its observable expression in IGC is strongly coupled to entropic changes (orientation constraints, packing and site-specificity). In other words, polar adsorption is not dominated by a large constant enthalpic baseline; it is dominated by how surface chemistry/morphology converts polar binding into organization costs, consistent with high $T_{int}^p$ values. This represents a $\mathcal{S}$-controlled polar compensation and quadratic morphology dependence.

The expressions of $T_{int}^p(\mathcal{S})$ and $\Delta H_a^p(\mathcal{S}, \Delta S = 0)$ are given by:

$$T_{int}^p(\mathcal{S}) = 4 \times 10^{-5}\mathcal{S}^2 + 0.560\mathcal{S} + 69.40, \quad (R^2 = 0.9366) \quad (45)$$

$$\Delta H_a^p(\mathcal{S}, \Delta S = 0) = 2 \times 10^{-5}\mathcal{S}^2 - 0.054\mathcal{S} + 31.16, \quad (R^2 = 0.8534) \quad (46)$$

These are major results because they demonstrate that polar enthalpy–entropy coupling is morphology-resolved. $T_{int}^{p}(\mathcal{S})$ is convex upward ($a_1^{p} > 0$). The positive quadratic coefficient indicates that the sensitivity of polar compensation strengthens at higher $\mathcal{S}$— meaning that as the copolymer becomes more porous/higher surface area, polar adsorption increasingly involves coupled stabilization + entropic penalty.

Physically, increasing $\mathcal{S}$ in hyper-cross-linked networks generally implies:

• more adsorption microenvironments (pore walls, edges, constrained pockets),

• increased heterogeneity of polarizable domains,

• increased probability of probe orientation locking and interfacial polarization.

All of these raise the entropic cost per unit enthalpic stabilization, hence increasing $T_{int}^{p}$ and producing an upward curvature with $S$.

This weak convexity of $\Delta H_a^{p}(\Delta S_a^{p} = 0)$ means that the baseline term has a small positive quadratic coefficient and a negative linear term, implying a shallow minimum *vs.* $\mathcal{S}$. This suggests a competition:

• at moderate $\mathcal{S}$, adding surface exposes a higher fraction of weaker polar sites (reducing baseline),

• at high $\mathcal{S}$, additional internal surfaces include more strongly polarizable/interactive environments (restoring baseline).

This again supports the ''site population shift'' interpretation: $\mathcal{S}$ increases do not simply add area; they change the distribution of polar adsorption environments.

It was proved that the mixed derivative:

$$\frac{\partial^2 \Delta H_a^{p}}{\partial(\Delta S_a^{p})\partial \mathcal{S}} = 8 \times 10^{-5}\mathcal{S} + 0.560 \tag{47}$$

is strictly positive over $\mathcal{S}$ range, meaning that increasing $\mathcal{S}$ systematically increases the strength of polar enthalpy–entropy coupling.

The polar adsorption on DVB-based copolymers exhibits a robust enthalpy–entropy compensation law, $\Delta H_a^{p} = T_{int}^{p}\Delta S_a^{p} + \Delta H_a^{p}(\Delta S_a^{p} = 0)$, with high linearity for all copolymers ($R^2 \approx 0.95$–$0.97$). The compensation temperature increases from poly(DVB) ($\sim$529 K) to the hyper-cross-linked/post-treated networks ($\approx$827–958 K), indicating that polar adsorption becomes increasingly governed by coupled energetic stabilization and entropic restriction, consistent with stronger orientation constraints and polarization-driven interfacial organization in higher-$\mathcal{S}$ architectures. Moreover, $T_{int}^{p}$ and $\Delta H_a^{p}(\Delta S_a^{p} = 0)$ display clear quadratic dependencies on SSA, demonstrating morphology-resolved compensation: specific surface area does not merely change adsorption magnitude but deterministically modulates the coupling between enthalpic and entropic contributions in polar adsorption.

(11) Morphology-resolved compensation

The specific surface area $\mathcal{S}$ controls both the slope and intercept of compensation lines. This converts $T_{int}$ from a single number into a morphology-dependent thermodynamic state function $T_{int}(\mathcal{S})$, and similarly for the enthalpic baseline.

• Classical compensation analyses treat each solid as one line with one $T_{int}$.

• It was shown that in DVB copolymers, $T_{int}$ itself is governed by $\mathcal{S}$, meaning adsorption thermodynamics are coupled to morphology in a measurable, predictive way.

The compensation law $\Delta H_a^{\chi}(\mathcal{S}) = T_{int}^{\chi}(\mathcal{S})\Delta S_a^{\chi} + \Delta H_a^{\chi}(\mathcal{S}, \Delta S_a^{\chi} = 0)$ establishes adsorption thermodynamics as a coupled function of entropy and copolymer morphology. Because both $T_{int}^{\chi}(\mathcal{S})$ and $\Delta H_a^{\chi}(\mathcal{S}, \Delta S = 0)$ are quadratic in $\mathcal{S}$, morphology modulates not only the magnitude of adsorption enthalpy but also the strength of enthalpy–entropy coupling. The mixed derivative $\partial^2 \Delta H_a^{\chi}/\left[\partial(\Delta S_a^{\chi})\partial \mathcal{S}\right] = \left(2a_1^{\chi}\mathcal{S} + b_1^{\chi}\right)$ provides an experimentally identified coupling constant linking surface architecture to the compensation slope. The sign and curvature of $a_1^{\chi}$ distinguish the adsorption regimes: dispersive adsorption exhibits convex strengthening of coupling with $\mathcal{S}$ ($a_1^{d} > 0$), consistent with confinement-driven ordering of *n*-alkanes, and polar adsorption also shows convex evolution ($a_1^{p} > 0$). Overall, the $\mathcal{S}$-resolved compensation framework provides a predictive thermodynamic map of adsorption on DVB-based copolymers.

This morphology-resolved thermodynamic structure is most clearly visualized through the three-dimensional compensation surfaces shown in Fig. 2, where adsorption enthalpy emerges as a continuous function of adsorption entropy and copolymer specific surface area for dispersive, polar, and total interaction channels.

Beyond visual representation, the compensation surfaces can be quantitatively characterized through their mixed derivatives and curvature, which define the strength of thermodynamic coupling between morphology and entropy. These parameters, reported in Table 8, provide a rigorous basis for comparing interaction channels and copolymer architectures.

**3.6.2. Quantitative metrics of the compensation surfaces.** While Fig. 2 provides a visual representation of morphology-resolved enthalpy–entropy compensation, a quantitative analysis was performed to characterize the underlying thermodynamic structure.

The coupling between morphology and compensation behavior is quantified by the mixed derivative:

$$\frac{\partial^2 \Delta H_a^{\chi}}{\partial S \partial \Delta S_a^{\chi}} = 2a_1^{\chi}S + b_1^{\chi} \tag{48}$$

which represents the sensitivity of the compensation slope to variations in specific surface area. This parameter defines a thermodynamic coupling strength linking polymer architecture to adsorption energetics.

The curvature of the compensation surface with respect to morphology is given by:

$$\frac{\partial^2 \Delta H_a^{\chi}}{\partial S^2} = 2a_1^{\chi}\Delta S_a^{\chi} + 2a_2^{\chi} \tag{49}$$

which captures second-order morphology effects and provides a quantitative measure of nonlinearity in adsorption thermodynamics.

Comparison across interaction channels reveals that dispersive contributions exhibit the strongest morphology-dependent coupling, while polar contributions show more moderate but structured variations. The total adsorption behavior reflects the combined influence of these contributions.

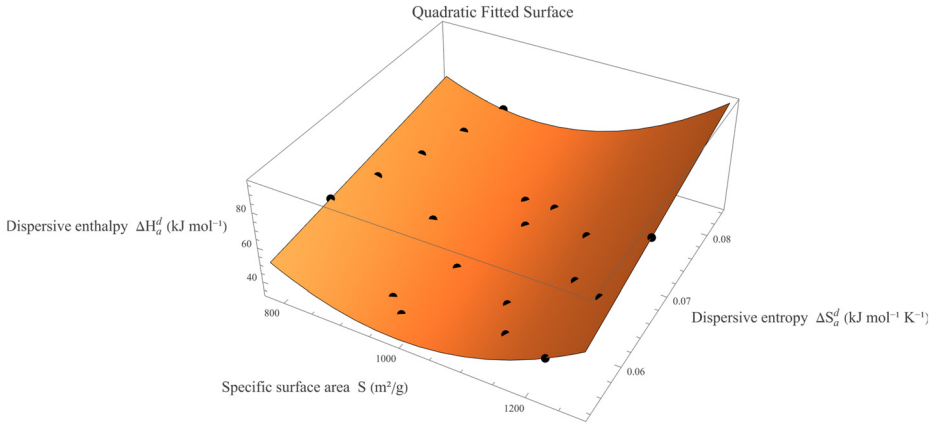


(a) Dispersive variations of $\Delta H_a^d(\mathcal{S}, \Delta S_a^d)$

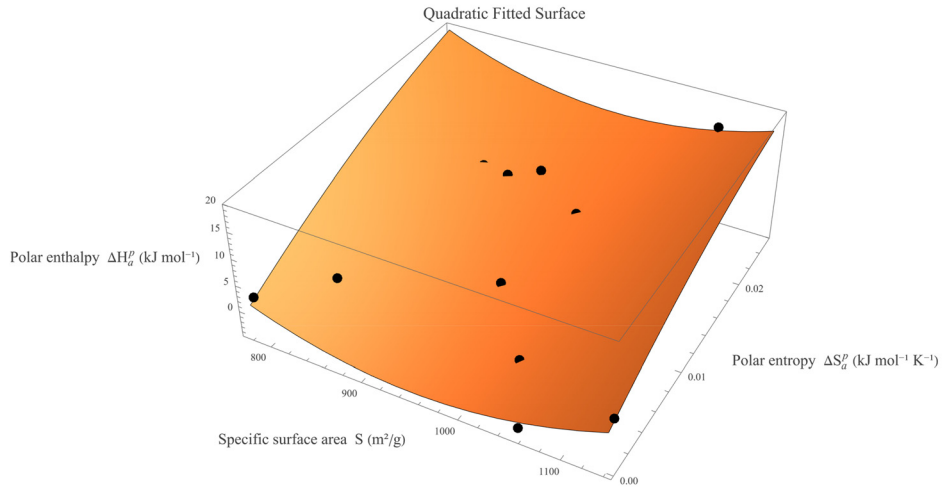


(b) Polar variations of $\Delta H_a^p(\mathcal{S}, \Delta S_a^p)$,

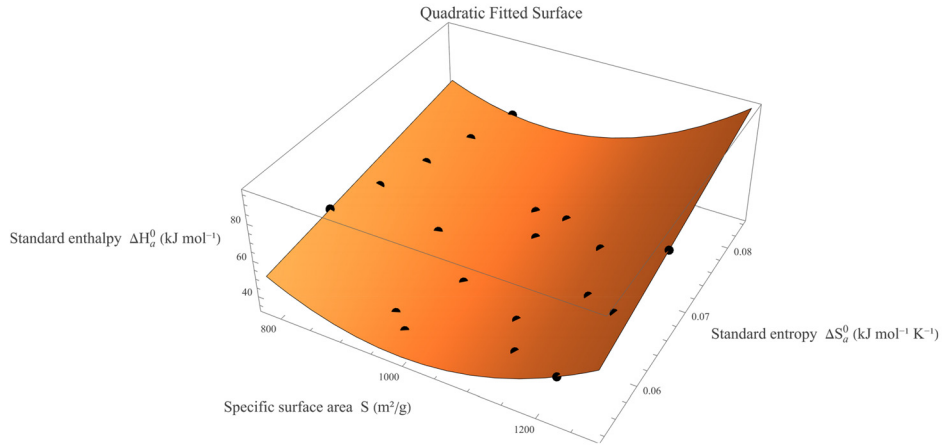


(c) Standard variations of $\Delta H_a^0(\mathcal{S}, \Delta S_a^{d0})$

Fig. 2 Morphology-resolved enthalpy–entropy compensation surface for adsorption on DVB-based copolymers. Three-dimensional thermodynamic representation of the adsorption enthalpy $\Delta H_a^\chi$ as a function of adsorption entropy $\Delta S_a^\chi$ and copolymer specific surface area $\mathcal{S}$ for the three interaction channels: (a) dispersive contribution ($\chi$ = *d*), (b) polar contribution ($\chi$ = *p*), and (c) total (standard) adsorption ($\chi$ = 0). For each interaction channel, the surfaces arise from the compensation relation $\Delta H_a^\chi(\mathcal{S}) = T_{int}^\chi(\mathcal{S})\Delta S_a^\chi + \Delta H_a^\chi(\mathcal{S}, \Delta S_a^\chi = 0)$, where both the intrinsic compensation temperature $T_{int}^\chi(\mathcal{S})$ and the reference enthalpy $\Delta H_a^\chi(\mathcal{S}, \Delta S = 0)$ are experimentally determined quadratic functions of the specific surface area.

A summary of the coupling coefficients and curvature parameters is provided in Table 10, enabling direct comparison between copolymers and interaction channels.

The planar linearity observed along the $\Delta S_a^\chi$ direction confirms strict local enthalpy–entropy compensation at fixed morphology, while the curvature along the $S$ axis reveals the deterministic influence of copolymer surface architecture on both the compensation slope and the enthalpic baseline. The geometry of the surfaces therefore reflects morphology-controlled thermodynamic coupling rather than independent energetic scaling. Differences between dispersive, polar, and total surfaces highlight the distinct physical origins of adsorption stabilization, configurational restriction, and morphology-dependent interaction constraints in DVB-based polymer networks.

Fig. 2 provides a unified thermodynamic visualization of adsorption on DVB-based copolymers by representing the adsorption enthalpy $\Delta H_a^\chi$ as a function of adsorption entropy $\Delta S_a^\chi$ and specific surface area $\mathcal{S}$, for the three interaction channels $\chi = d$ (dispersive), $p$ (polar), and 0 (total/standard). In all cases, the surfaces confirm that adsorption does not evolve on a single universal compensation line; rather, each copolymer morphology corresponds to a distinct local compensation behavior, and the ensemble of copolymers forms a continuous thermodynamic ''surface'' in the $(\mathcal{S}, \Delta S)$ space.

(i) Common structural feature: linearity along $\Delta S$ and morphology-dependent slope

For each channel, cross-sections at fixed $S$ appear as straight lines along the $\Delta S$ direction, demonstrating strict enthalpy–entropy compensation:

$$\Delta H_a^\chi = T_{int}^\chi(\mathcal{S})\Delta S_a^\chi + \Delta H_a^\chi\left(\mathcal{S}, \Delta S_a^\chi = 0\right) \qquad (50)$$

Thus, the 3D representation makes two points simultaneously: (1) compensation is locally linear for a given morphology, and (2) both the slope $T_{int}^\chi$ and intercept $\Delta H_a^\chi\left(\mathcal{S}, \Delta S_a^\chi = 0\right)$ vary with $\mathcal{S}$, which is why the global response is a surface rather than a single plane.

(ii) Dispersive surface: ''mechanistic purity'' and strong morphology-driven coupling

The dispersive surface (Fig. 2a), constructed from *n*-alkane adsorption, is typically the most ordered and coherent. This reflects the quasi-ideal character of dispersion-dominated adsorption, where chemical specificity is minimal and the dominant control parameters are polarizability scaling (enthalpic) and packing/order constraints (entropic). The pronounced curvature of the dispersive surface along $S$ indicates that increasing specific surface area strongly enhances enthalpy–entropy coupling (*i.e.*, it alters the compensation slope). Mechanistically, this is consistent with $\mathcal{S}$ increases being accompanied by changes in the distribution of adsorption microenvironments (*e.g.*, higher fraction of confined, high-curvature, or microporous domains), which penalize configurational freedom of the alkyl chain as adsorption strength increases. In this sense, the dispersive surface encodes a transition from ''more open'' segmental adsorption to increasingly confinement-controlled adsorption regimes as $\mathcal{S}$ grows.

(iii) Polar surface: morphology-sensitive but reflecting interaction-mode diversity

The polar surface (Fig. 2b) remains strongly structured, confirming robust compensation, but it is expected to appear less ''ideal'' than the dispersive case because polar probes can engage multiple interaction modes (dipole–induced dipole, dipole–dipole, polarization of aromatic domains, and potential heterogeneity of adsorption sites). The curvature of the polar surface along $\mathcal{S}$ demonstrates that SSA governs not only the magnitude of polar stabilization but the degree to which entropic penalties accompany it—*i.e.*, morphology controls the balance between energetic gain and orientational/conformational restriction. A key implication of the polar surface is that increases in $\mathcal{S}$ do not simply increase adsorption strength; rather, they tend to increase the coupling between stabilization and ordering, consistent with more heterogeneous and more strongly structuring environments at high accessible surface area.

(iv) Total (standard) surface: emergent superposition and ''intermediate'' thermodynamic regime

The total adsorption surface (Fig. 2c) represents the combined effect of dispersive and polar contributions and therefore typically occupies an intermediate thermodynamic regime between Fig. 2a and b. Its geometry reflects an emergent balance: the dispersive channel imposes strong packing/confinement contributions, while the polar channel adds interaction-mode diversity and site sensitivity. The resulting surface demonstrates that the observed total adsorption thermodynamics cannot be fully rationalized by either contribution alone; rather, total adsorption is a structured thermodynamic response whose morphology dependence reflects the joint action of dispersion cohesion and polarity-driven ordering.

The specific surface area then acts as a thermodynamic control variable, not merely a geometric descriptor. Across all three surfaces, the fact that (i) the local compensation relation remains linear, but (ii) the global behavior forms a curved surface in $(\mathcal{S}, \Delta S)$ space, provides direct evidence that the intrinsic temperature $T_{int}^\chi$ and the enthalpic baseline $\Delta H_a^\chi\left(\mathcal{S}, \Delta S_a^\chi = 0\right)$ are morphology-dependent state descriptors. In other words, the DVB network morphology controls the thermodynamic pathway of adsorption by tuning how strongly energetic stabilization is coupled to entropic restriction. This observation is central to the present work because it transforms the classical compensation concept—from a single line for a given material—into a predictive morphology-resolved framework.

The introduction of explicit thermodynamic coupling metrics reveals that adsorption energetics are governed by a structured interplay between surface morphology and thermal fluctuations, rather than by independent energetic contributions. This finding provides a quantitative foundation for interpreting adsorption behavior in complex polymer networks

## 4. Thermodynamic and morphological implications of the compensation surfaces

The morphology-resolved compensation surfaces derived from the inverse gas chromatography measurements provide a unified

thermodynamic perspective on adsorption phenomena in DVB-based copolymer networks. Rather than representing adsorption energetics as isolated parameter sets, the three-dimensional framework reveals that adsorption enthalpy, entropy, and specific surface area are intrinsically coupled state variables governed by deterministic relations. This finding has important conceptual implications for polymer surface thermodynamics.

First, the preservation of strict linearity between $\Delta H_a^\gamma$ and $\Delta S_a^\gamma$ at fixed morphology confirms that enthalpy–entropy compensation constitutes a fundamental invariant of probe–polymer interactions. The observed compensation behavior is therefore not an empirical correlation but a direct consequence of the balance between energetic stabilization and configurational restriction. The intrinsic temperature $T_{int}^\gamma$ acquires a clear physical meaning as a morphology-controlled parameter reflecting the energetic cost of entropy reduction during adsorption.

Second, the quadratic dependence of both $T_{int}^\gamma(\mathcal{S})$ and $\Delta H_a^\gamma\left(\mathcal{S}, \Delta S_a^\gamma = 0\right)$ demonstrates that specific surface area operates as a genuine thermodynamic control variable rather than a purely geometric descriptor. Variations in $\mathcal{S}$ modify not only the magnitude of adsorption energies but also the coupling strength between enthalpic and entropic contributions. In polymeric networks, where $\mathcal{S}$ reflects cross-linking density, pore accessibility, and topological constraints, morphology directly governs the thermodynamic pathway of adsorption.

Third, the constant mixed derivatives obtained for both adsorption distances and dispersive surface energies reveal a deeper thermomechanical origin of adsorption thermodynamics. The bilinear energetic structure indicates that temperature and morphology contribute symmetrically to adsorption behavior, consistent with adsorption being regulated by thermally activated fluctuations within mechanically constrained polymer networks. This interpretation links microscopic interaction potentials with macroscopic morphological descriptors.

Finally, the continuity of the compensation surfaces across dispersive, polar, and total interaction channels suggests that adsorption thermodynamics in complex polymer systems can be described within a unified energetic landscape. Differences between interaction channels reflect variations in interaction mechanisms rather than breakdown of the thermodynamic framework itself. The morphology-resolved compensation approach therefore provides a generalizable description applicable to cross-linked, hyper-cross-linked, and heterogeneous polymeric solids.

### 4.1. Scope and limitations of the thermomechanical framework

The thermomechanical framework developed in this work provides a unified description of adsorption phenomena on DVB-based copolymers; however, its applicability is subject to certain conditions.

The model is particularly well suited for cross-linked and hyper-cross-linked polymeric systems, where adsorption is dominated by reversible physisorption and where the specific surface area reflects the accessible morphology of the network. Under these conditions, the coupling between temperature, morphology, and adsorption energetics can be described by deterministic relations.

However, the approach may be less applicable to systems exhibiting fundamentally different adsorption mechanisms. In particular, materials dominated by strong chemisorption, highly crystalline solids with discrete adsorption sites, or systems undergoing significant structural rearrangement or swelling during adsorption may deviate from the assumptions of the model. Similarly, highly heterogeneous materials for which a single specific surface area does not adequately describe the accessible interface may require more complex descriptors.

The present formulation also assumes thermodynamic equilibrium and negligible kinetic limitations, conditions that are generally satisfied under inverse gas chromatography at infinite dilution but may not hold in dynamic or high-coverage regimes.

Despite these limitations, the framework provides a robust and generalizable basis for interpreting adsorption thermodynamics in a wide range of polymeric and porous materials and offers a foundation for future extensions to more complex systems.

These results highlight that the thermomechanical framework captures both first-order adsorption behavior and second-order morphology effects, thereby offering a unified description of adsorption phenomena across structurally diverse copolymer systems.

The emergence of continuous thermodynamic surfaces in $(\mathcal{S}, \Delta S, \Delta H)$ space establishes adsorption as a morphology-governed process, bridging molecular interactions and macroscopic surface descriptors within a unified theoretical framework.

## 5. Conclusions

This study provides a new thermodynamic, thermomechanical, and chemical characterization of solvent adsorption on DVB-based copolymers and hyper-cross-linked resins using inverse gas chromatography within the Hamieh framework. By systematically analyzing adsorption free energy, adsorption distance, dispersive surface energy, and specific surface area, a unified description of interfacial behavior has been established in which temperature and surface morphology act as intrinsically coupled variables.

The adsorption distance between solvent molecules and the copolymer surface was shown to follow a bilinear thermomechanical law, $r_{X/S}(T, \mathcal{S})$, with experimentally determined first and mixed second derivatives. This demonstrates that thermal dilation of the adsorption configuration is directly modulated by the specific surface area, revealing a clear morphology–temperature coupling. The sign and magnitude of the coupling coefficient distinguish dispersion-dominated adsorption on rigid aromatic domains from polarity-driven adsorption on more compliant and heterogeneous sites.

An analogous bilinear dependence was established for the London dispersive surface energy, $\gamma_s^d(T, \mathcal{S})$. The dispersive surface entropy and the extrapolated surface energy at zero surface area both vary linearly with temperature, confirming that dispersive interactions are governed by a balance between

energetic stabilization and entropic weakening. The parallel bilinear forms of $r_{X/S}(T,\mathcal{S})$ and $\gamma_s^d(T,\mathcal{S})$ demonstrate that adsorption geometry and interaction energy are governed by the same underlying thermomechanical principles.

Enthalpy–entropy compensation analysis revealed that the intrinsic compensation temperature and enthalpic baseline are morphology-dependent quantities governed by quadratic scaling with specific surface area. The deterministic variation of compensation parameters across copolymer architectures demonstrates that adsorption thermodynamics are fundamentally controlled by structural constraints imposed by polymer cross-linking and network topology. The compensation framework therefore acquires a morphology-resolved interpretation, linking microscopic energetic balance to macroscopic surface properties.

Overall, the present methodology establishes a unified molecular-thermodynamic description of adsorption on polymeric solids, enabling the direct extraction of adsorption distances, dispersive surface energies, and morphology-dependent thermodynamic invariants from retention measurements. The approach offers a robust route toward physically interpretable surface characterization of complex polymeric materials.

## Conflicts of interest

The author declares that there is no conflict of interest.

## Data availability

All data generated or analyzed during this study are included in this published article and its supplementary information (SI). The supplementary information contains (i) the textural properties of the investigated copolymers, including BET specific surface areas and microporous volumes; (ii) the temperature-dependent total, London dispersive, and polar adsorption free energies of the probe solvents; (iii) the corresponding adsorption enthalpies, entropies, and intrinsic temperatures derived from thermodynamic analyses; and (iv) the regression equations describing the dependence of these thermodynamic parameters on temperature and polymer specific surface area, together with the associated statistical fitting coefficients. See DOI: https://doi.org/10.1039/d6ma00325g.

## Acknowledgements

This research did not receive any specific grant from funding agencies in the public, commercial, or not-for-profit sectors.

## References

1 L. Ding, H. Gao, F. Xie, W. Li, H. Bai and L. Li, Porosity-Enhanced Polymers from Hyper-Cross-Linked Polymer Precursors, *Macromolecules*, 2017, **50**(3), 956–962, DOI: 10.1021/acs.macromol.6b02715.

2 L. Jia, J. Ma, Q. Shi and C. Long, Prediction of adsorption equilibrium of VOCs onto hyper-cross-linked polymeric resin using inverse gas chromatography, *Environ. Sci. Technol.*, 2017, **51**, 522–530.

3 H. Benguergoura, A. Allel, W. S. Saeed and T. Aouak, Capillary column IGC for thermodynamic parameters of poly(styrene-*co*-butadiene) rubber systems, *Arabian J. Chem.*, 2021, **14**, 103040, DOI: 10.1016/j.arabjc.2021.103040.

4 G. Ovejero, P. Pérez, M. D. Romero, I. Díaz and E. Díez, SEBS triblock copolymer–solvent interaction parameters from IGC measurements, *Eur. Polym. J.*, 2009, **45**(2), 590–594, DOI: 10.1016/j.eurpolymj.2008.11.022.

5 S. Yamada, T. Kajita, M. Nishimoto, J. Horiuchi, Y. Fujii, K. Sakaguchi, K. Hattori, H. Tamura, T. Kano, T. Sakai and A. Noro, Next-Generation Structural Adhesives Composed of Epoxy Resins and Hydrogen-Bonded Styrenic Block Polymer-Based Thermoplastic Elastomers, *ACS Appl. Mater. Interfaces*, 2024, **16**(47), 65270–65280, DOI: 10.1021/acsami.4c12540.

6 M. R. Reed, E. R. Belden, N. K. Kazantzis, M. T. Timko and B. Castro-Dominguez, Thermodynamic and economic analysis of a deployable and scalable process to recover Monomer-Grade styrene from waste polystyrene, *Chem. Eng. J.*, 2024, **492**, 152079, DOI: 10.1016/j.cej.2024.152079.

7 H. Liu, L. Wang, J. Zhang, X. Liang and C. Long, Mechanistic insights into and modeling the effects of relative humidity on low-concentration VOCs adsorption on hyper-cross-linked polymeric resin by inverse gas chromatography, *J. Hazard. Mater.*, 2021, **418**, 126335, DOI: 10.1016/j.jhazmat.2021.126335.

8 L. Jia, X. Song, J. Wu and C. Long, Surface properties of hyper-cross-linked polymeric resins using inverse gas chromatography: effect of post-cross-linking solvents, *J. Phys. Chem. C*, 2015, **119**(37), 21404–21412, DOI: 10.1021/acs.jpcc.5b07110.

9 E. Díez, G. Ovejero, M. D. Romero and I. Díaz, Polymer–solvent interaction parameters of styrene–butadiene–styrene (SBS) rubbers by IGC, *Fluid Phase Equilib.*, 2011, **308**(1–2), 107–113, DOI: 10.1016/j.fluid.2011.06.018.

10 T. Hamieh, New Advances on the Dispersive and Polar Surface Properties of Poly(styrene-*co*-butadiene) Using Inverse Gas Chromatography, *Polymers*, 2024, **16**, 3233, DOI: 10.3390/polym16233233.

11 T. Hamieh and V. Y. Gus'kov, Surface Thermodynamic Properties of Styrene–Divinylbenzene Copolymer Modified by Supramolecular Structure of Melamine Using Inverse Gas Chromatography, *Chemistry*, 2024, **6**, 830–851, DOI: 10.3390/chemistry6050050.

12 T. Hamieh and V. Y. Gus'kov, Effect of Temperature on Adhesion Work of Model Organic Molecules on Modified Styrene–Divinylbenzene Copolymer Using Inverse Gas Chromatography, *Crystals*, 2025, **15**, 490, DOI: 10.3390/cryst15060490.

13 T. Hamieh and V. Y. Gus'kov, Determination of Surface Physicochemical Parameters of Styrene–Divinylbenzene Copolymer Modified by 5-Fluouracil Using Inverse Gas Chromatography, Preprints, 2025, p. 041864, DOI: 10.20944/preprints202504.1864.v1.

14 T. Hamieh and V. Y. Gus'kov, Thermodynamic Surface and Interface Characterization of 5-Fluorouracil-Modified S-DVB

Copolymer: Deconvolution of London Dispersive and Polar Components Using a Novel Thermal Approach, *Surf. Interfaces*, 2025, DOI: 10.2139/ssrn.5342827.

15 F. Thielmann and D. J. Burnett, Applications of inverse gas chromatography in materials science, *J. Colloid Interface Sci.*, 2013, **393**, 163–176.

16 D. G. Gray and G. M. Dorris, Adsorption characteristics of polymeric surfaces by inverse gas chromatography, *J. Colloid Interface Sci.*, 1979, **70**, 309–316.

17 A. Nastasovic, Surface characterization of polymers by inverse gas chromatography, *J. Serb. Chem. Soc.*, 2007, **72**(4), 403–406, DOI: 10.2298/JSC0704403N.

18 S. Dong, M. Brendlé and J. B. Donnet, Influence du traitement thermique sur les propriétés de surface des fibres de carbone ex-mésophase, *J. Chim. Phys.*, 1991, **88**, 1831–1847, DOI: 10.1051/jcp/1991881831.

19 J. Sygusch, R. Duempelmann, R. Meyer, K. Adamska, B. Strzemiecka, D. Enke, M. Rudolph and E. Brendlé, Reproducibility of inverse gas chromatography under infinite dilution: interlaboratory study, *J. Chromatogr. A*, 2024, **1714**, 464526, DOI: 10.1016/j.chroma.2023.464526.

20 S. Saini, S. Chatterjee and D. Dutta, Inverse Gas Chromatography: A Powerful Tool to Characterize Polymer Surface Energetics and Acid–Base Properties, *Adv. Colloid Interface Sci.*, 2020, **276**, 102077, DOI: 10.1016/j.cis.2019.102077.

21 J.-B. Donnet, S. Park and H. Balard, Evaluation of specific interactions of solid surfaces by inverse gas chromatography, *Chromatographia*, 1991, **31**, 434–440, DOI: 10.1007/BF02262385.

22 E. Brendlé and E. Papirer, A New Topological Index for Molecular Probes Used in Inverse Gas Chromatography, *J. Colloid Interface Sci.*, 1997, **194**, 217–224, DOI: 10.1006/jcis.1997.5105.

23 E. Brendlé and E. Papirer, A New Topological Index for Molecular Probes Used in Inverse Gas Chromatography for the Surface Nanorugosity Evaluation, *J. Colloid Interface Sci.*, 1997, **194**, 207–216, DOI: 10.1006/jcis.1997.5104.

24 A. Voelkel, B. Strzemiecka, K. Adamska and K. Milczewska, Inverse gas chromatography as a source of physiochemical data, *J. Chromatogr. A*, 2009, **1216**, 1551–1566.

25 P. Mukhopadhyay and H. P. Schreiber, Aspects of acid–base interactions and use of inverse gas chromatography, *Colloids Surf., A*, 1995, **100**, 47–71.

26 A. F. Kishway, R. M. Abouomar, M. Bakry, M. A. Ebiad and K. A. Khalil, Investigation of thermodynamic and solubility properties of poly(4-methyl styrene-*alt*-maleic anhydride) and poly(4-methyl styrene-*alt*-*n*-propyl maleimide) copolymers by inverse gas chromatography, *J. Chromatogr. A*, 2025, **1745**, 465744.

27 T. Hamieh, Exploring the application of advanced chromatographic methods to characterize the surface physicochemical properties and transition phenomena of polystyrene-*b*-poly(4-vinylpyridine), *Molecules*, 2024, **29**(20), 4812.

28 T. Hamieh, Some irregularities in the evaluation of surface parameters of solid materials by inverse gas chromatography, *Langmuir*, 2023, **39**(48), 17059–17070.

29 A. Kondor and D. J. Burnett, Correct specific retention volume determination in inverse gas chromatography, *J. Chromatogr. A*, 2023, **1700**, 464009.

30 A. Voelkel, Inverse Gas Chromatography: Characterization of Polymers, Fibers, Modified Silicas, and Surfactants, *Crit. Rev. Anal. Chem.*, 1991, **22**, 411–439, DOI: 10.1080/10408349108051641.

31 S. K. Papadopoulou and C. Panayiotou, Assessment of the thermodynamic properties of poly(2,2,2-trifluoroethyl methacrylate) by inverse gas chromatography, *J. Chromatogr. A*, 2014, **1324**, 207–214, DOI: 10.1016/j.chroma.2013.11.044.

32 T. Hamieh, Study of the temperature effect on the surface area of model organic molecules, the dispersive surface energy and the surface properties of solids by inverse gas chromatography, *J. Chromatogr. A*, 2020, **1627**, 461372, DOI: 10.1016/j.chroma.2020.461372.

33 T. Hamieh, New Methodology to Study the Dispersive Component of the Surface Energy and Acid–Base Properties of Silica Particles by Inverse Gas Chromatography at Infinite Dilution, *J. Chromatogr. Sci.*, 2021, **60**, 126–142, DOI: 10.1093/chromsci/bmab066.

34 V. Gutmann, *The Donor-Acceptor Approach to Molecular Interactions*, Plenum, New York, NY, USA, 1978.

35 F. L. Riddle and F. M. Fowkes, Spectral shifts in acid-base chemistry. van der Waals contributions to acceptor numbers, Spectral shifts in acid-base chemistry. 1. van der Waals contributions to acceptor numbers, *J. Am. Chem. Soc.*, 1990, **112**, 3259–3264, DOI: 10.1021/ja00165a001.

36 G. M. Dorris and D. G. Gray, Adsorption of n-alkanes at zero surface coverage on cellulose paper and wood fibers, *J. Colloid Interface Sci.*, 1980, **77**, 353–362, DOI: 10.1016/0021-9797(80)90304-5.

37 T. Hamieh, A. A. Ahmad, T. Roques-Carmes and J. Toufaily, New approach to determine the surface and interface thermodynamic properties of H-β-zeolite/rhodium catalysts by inverse gas chromatography at infinite dilution, *Sci. Rep.*, 2020, **10**, 20894, DOI: 10.1038/s41598-020-78071-1.

38 F. M. Fowkes in *Surface and Interfacial Aspects of Biomedical Polymers*, ed. J. D. Andrade, Plenum Press, New York, NY, USA, 1985, vol. I, pp. 337–372.

39 T. Hamieh, New physicochemical methodology for the determination of the surface thermodynamic properties of solid particles, *Appl. Chem.*, 2023, **3**, 229–255, DOI: 10.3390/appliedchem3020015.

40 T. Hamieh, New Progress on London Dispersive Energy, Polar Surface Interactions, and Lewis's Acid–Base Properties of Solid Surfaces., *Molecules*, 2024, **29**, 949, DOI: 10.3390/molecules29050949.

41 T. Hamieh, London Dispersive and Lewis Acid-Base Surface Energy of 2D Single-Crystalline and Polycrystalline Covalent Organic Frameworks., *Crystals*, 2024, **14**, 148, DOI: 10.3390/cryst14020148.

42 Y. Wang, C. Narita, X. Xu, H. Honma, Y. Himeda and K. Yamada, Controlling the ordered transition of PS-*b*-P4VP block copolymer ultrathin films by solvent annealing., *Mater. Chem. Phys.*, 2020, **239**, 122072, DOI: 10.1016/j.matchemphys.2019.122072.

43 H. Hasegawa and T. Hashimoto, Morphology of block copolymers and mixtures of block copolymers at free surfaces., *Polymer*, 1992, **33**, 475–487.
44 D. H. Lee, H. Cho, S. Yoo and S. Park, Ordering evolution of block copolymer thin films upon solvent-annealing process., *J. Colloid Interface Sci.*, 2012, **383**, 118–123.
45 N. Yan and Y. Wang, Reversible switch between the nanoporous and the nonporous state of amphiphilic block copolymer films regulated by selective swelling., *Soft Matter*, 2015, **11**, 6927–6937.
46 S. A. Shamsudin, T. Mikihito and H. Hirokazu, Controlling ordered structures of PS-*b*-P2VP block copolymer thin film by tuning solvent evaporation rate., *Macromol. Symp.*, 2017, **371**, 75–83.
47 W. Zha, C. D. Han, D. H. Lee, S. H. Han, J. K. Kim, J. H. Kang and C. Park, Origin of the difference in Order−Disorder transition temperature between polystyrene-*block*-poly(2-vinylpyridine) and polystyrene-*block*-poly(4-vinylpyridine) copolymers., *Macromolecules*, 2007, **40**, 2109–2119.
48 L. Hoebus, M. J. Tavaststjerna and S. J. Garcia, Mobility of antifreeze proteins as a key factor in their use to control ice growth on surfaces and polymers, *Appl. Surf. Sci. Adv.*, 2025, **28**, 100790, DOI: 10.1016/j.apsadv.2025.100790.
49 M. Rezaei, S. M. Rabiee, R. Jamaati and S. Rahmani, Surface modification of AISI 316 L stainless steel with polyvinyl alcohol/chitosan/sol-gel bioactive glass coating by electrospinning method, *Appl. Surf. Sci. Adv.*, 2025, **28**, 100801, DOI: 10.1016/j.apsadv.2025.100801.
50 P. P. Angelopoulou, I. Moutsios, G. M. Manesi, D. A. Ivanov, G. Sakellariou and A. Avgeropoulos, Designing high χ copolymer materials for nanotechnology applications: A systematic bulk vs. thin films approach, *Prog. Polym. Sci.*, 2022, **135**, 101625, DOI: 10.1016/j.progpolymsci.2022.101625.
51 C. Cummins, G. Pino, D. Mantione and G. Fleury, Engineering block copolymer materials for patterning ultra-low dimensions, *Mol. Syst. Des. Eng.*, 2020, **5**, 1642–1657.
52 S. Kouser, A. Prabhu, S. Sheik, K. Prashantha, G. K. Nagaraja, J. N. D'souza, K. M. Navada and D. J. Manasa, Chitosan functionalized halloysite nanotube/poly (caprolactone) nanocomposites for wound healing application, *Appl. Surf. Sci. Adv.*, 2021, **6**, 100158, DOI: 10.1016/j.apsadv.2021.100158.
53 P. Kannan, A. Varghese, K. Palanisamy and A. S. Abousalem, Probing the effect of newly synthesized phenyltrimethylammonium tetrachloroaluminate ionic liquid as an inhibitor for carbon steel corrosion, *Appl. Surf. Sci. Adv.*, 2021, **6**, 100150, DOI: 10.1016/j.apsadv.2021.100150.
54 V. Donchak, Y. Stetsyshyn, M. Bratychak, G. Broza, K. Harhay, N. Stepina, M. Kostenko and S. Voronov, Nanoarchitectonics at surfaces using multifunctional initiators of surface-initiated radical polymerization for fabrication of the nanocomposites, *Appl. Surf. Sci. Adv.*, 2021, **5**, 100104, DOI: 10.1016/j.apsadv.2021.100104.
55 T. Hamieh, Inverse Gas Chromatography to Characterize the Surface Properties of Solid Materials, *Chem. Mater.*, 2024, **36**, 2231–2244, DOI: 10.1021/acs.chemmater.3c03091.
56 T. Hamieh, Effect of Tacticity on London Dispersive Surface Energy, Polar Free Energy and Lewis Acid-Base Surface Energies of Poly Methyl Methacrylate by Inverse Gas Chromatography, *Macromol*, 2024, **4**, 356–375, DOI: 10.3390/macromol4020020.
57 T. Hamieh, The Effect of Temperature on the London Dispersive and Lewis Acid-Base Surface Energies of Polymethyl Methacrylate Adsorbed on Silica by Inverse Gas Chromatography, *Thermo*, 2024, **4**, 202–221, DOI: 10.3390/thermo4020012.
58 T. Hamieh, Temperature Dependence of the Polar and Lewis Acid–Base Properties of Poly Methyl Methacrylate Adsorbed on Silica *via* Inverse Gas Chromatography, *Molecules*, 2024, **29**, 1688, DOI: 10.3390/molecules29081688.
59 T. Hamieh, Thermodynamic and Molecular Analysis of Polar Adsorption Enthalpy: New Model of Lewis Acid–Base Energetics at Solid Surfaces, *Langmuir*, 2026, **42**(4), 3539–3561, DOI: 10.1021/acs.langmuir.5c05989.
60 T. Hamieh, Unified Thermodynamic Modeling of Adsorption and London Dispersive Surface Energy on Rh-Modified H-β Zeolite: Coupled Effects of Temperature, Metal Loading, and Specific Surface Area, *Hybrid Adv.*, 2026, **12**, 100614, DOI: 10.1016/j.hybadv.2026.100614.
61 T. Hamieh, New breakthrough in interfacial characterization: concept of molecular surface area of molecules from a static geometric constant into a dynamic thermodynamic property using inverse gas chromatography, *J. Chromatogr. A*, 2026, **1765**, 466542, DOI: 10.1016/j.chroma.2025.466542.
62 T. Hamieh, A General Thermodynamic Law for Adsorption Geometry at Polymer/Oxide Interfaces: Lewis Acid–Base Energetics and Interfacial Cooperativity, *Mater. Des.*, 2026, **264**, 115729, DOI: 10.1016/j.matdes.2026.115729.
63 L. Jia, X. Song, J. Wu and C. Long, Surface Properties of Hyper-Cross-Linked Polymeric Resins Using Inverse Gas Chromatography: Effect of Post-Cross-Linking Solvents, *J. Phys. Chem. C*, 2015, **119**, 21404–21412, DOI: 10.1021/acs.jpcc.5b07110.
64 C. Kemball and E. K. Rideal, The adsorption of vapours on mercury I) Non –polar substances, *Proc. R. Soc. London, Ser. A*, 1946, **187**, 53–73.
65 J. H. De Boer and S. Kruyer, Entropy and mobility of adsorbed molecules I) Procedure; atomic gases on charcoal, *Proc. K. Ned. Akad. Wet.*, 1952, **5**, 451–463.